

Resolving carbonate platform geometries on the Island of Bonaire, Caribbean Netherlands through semi-automatic GPR facies classification

R.D. Bowling, J.C. Laya and M.E. Everett

Department of Geology and Geophysics, Texas A&M University, College Station, TX 77843, USA. E-mail: rbowling42@tamu.edu

Accepted 2018 May 1. Received 2018 April 10; in original form 2017 December 18

SUMMARY

The study of exposed carbonate platforms provides observational constraints on regional tectonics and sea-level history. In this work Miocene-aged carbonate platform units of the Seroe Domi Formation are investigated on the island of Bonaire, located in the Southern Caribbean. Ground penetrating radar (GPR) was used to probe near-surface structural geometries associated with these lithologies. The single cross-island transect described herein allowed for continuous mapping of geologic structures on kilometre length scales. Numerical analysis was applied to the data in the form of *k*-means clustering of structure-parallel vectors derived from image structure tensors. This methodology enables radar facies along the survey transect to be semi-automatically mapped. The results provide subsurface evidence to support previous surficial and outcrop observations, and reveal complex stratigraphy within the platform. From the GPR data analysis, progradational clinoform geometries were observed on the northeast side of the island which support the tectonics and depositional trends of the region. Furthermore, several leeward-side radar facies are identified which correlate to environments of deposition conducive to dolomitization via reflux mechanisms.

Key words: Ground penetrating radar; Image processing; Sedimentary basin processes; Persistence, memory, correlations, clustering.

1 INTRODUCTION

The variety of carbonate deposits around the globe has provided an endless source of research topics in sedimentology and stratigraphy, including depositional history, platform geometry, geochemistry, etc. (Eberli & Ginsburg 1989; Kenter 1990; Read 1995; Mutti *et al.* 1997; Pomar 2001; Brandano & Corda 2002; Della Porta *et al.* 2004). Given that the origins of carbonate rocks are directly tied to past ocean conditions (James & Jones 2016), a better understanding of how they form can provide important information about sea-level history, paleoclimate, as well as regional tectonics. However, most of the previous studies have taken place in areas that have been in tectonically stable (e.g. The Bahamas) with a single control, such as sea-level history, determining depositional or stratigraphic architecture. Few of the previously studied platforms record the interaction of both eustasy and tectonic evolution (e.g. Barbados, Dominican Republic and Jamaica).

In the southern Caribbean, the island of Bonaire presents a spectacular set of exposures that make this area an ideal location to understand complex controls including sea-level history, climate and tectonic relationships, based on geometrical features. The primary purpose of this paper is to investigate how such controls have

shaped the island's present-day carbonate morphology and stratigraphic geometries. This is important for understanding the history and evolution of Caribbean region at large, including allogenic controls on carbonate deposits.

Many authors have described terraced morphology on Bonaire and the surrounding ABC (Aruba, Bonaire and Curacao) islands (Alexander 1961; de Buissonjé, 1964, 1974; Bandoian & Murray 1974; Schellmann *et al.* 2004; Muhs *et al.* 2012). This morphology is the product of exposure, marine erosion and depositional episodes that have not been extensively studied on the island. Recent research (Laya *et al.* 2018) suggests that the terraces on the island are less significant to the stratigraphy than has been pointed out before. Instead, we focus on examining the internal architecture of the strata and regional trends through the use of ground penetrating radar (GPR) to provide more relevant information about depositional episodes. In particular, this study examines more closely the various geometries and stratigraphic architecture of the Seroe Domi Formation, which describes a period of carbonate progradation on the island (Laya *et al.* 2018).

GPR has been successfully used to provide high-resolution near-surface imaging of carbonate formations (Martinez *et al.* 1998; Asprien & Aigner 2000; Asprien *et al.* 2009; Jorry & Bièvre 2011; Forte *et al.* 2012; Menezes *et al.* 2016). Reflections observed in

GPR data have been shown to correlate with observable features in carbonates at the outcrop-scale (Martinez *et al.* 1998; Jorry & Bièvre 2011). GPR has particular utility in determining subsurface information in regions where little to no outcrop evidence exists. In this study we extend the use of GPR in carbonates to image subsurface geologic structures over km-scale distances on Bonaire. Numerical techniques, which involve a detailed identification of the structural trends implied by the GPR data, are herein utilized to provide semi-automatic classification of radar facies utilized in geologic interpretation. This study takes advantage of the high resolution (submetre) nature of GPR data to describe individual structures that are laterally continuous on the order of 10s of m. The GPR data set used in this study represents one of a very few geophysical data sets collected on Bonaire (e.g. de Kleine & Bakker 2009) and, to our knowledge, is the first one aimed specifically at furthering the understanding of the overall geological evolution of the island.

2 GEOGRAPHIC AND GEOLOGIC SETTING

The island of Bonaire is located in the Southern Caribbean as part of the Leeward Antilles islands. Formerly part of the Netherlands Antilles, Bonaire is now a special municipality within the Netherlands. The island is located approximately 90 km north of the Venezuelan coast, and consequently is infrequently affected by severe tropical storms or hurricanes seen farther northwest in the Caribbean (Lugo *et al.* 2000). Moreover, the island is quite arid with the mean yearly rainfall being on the order of 500 mm (Stoffers 1956).

Geologically, the island is composed of a Cretaceous volcanic basement overlain by Neogene to Holocene carbonate rocks and sediments (de Buissonjé 1974; Laya *et al.* 2018). The basement has been attributed to volcanism resulting from the shallow subduction of the Caribbean plate beneath the South American plate that created the South Caribbean deformed belt and the Leeward Antilles ridge (Van der Hilst & Mann 1994; Hippolyte & Mann 2011). Uplift and erosion caused deposition of clastic sediments on the volcanic slopes, with consistent deposition through carbonate production systems beginning sometime in the middle Eocene (Pijpers 1933; Bandoian & Murray 1974; de Buissonjé 1974). The Miocene through Pliocene saw the deposition of extensive carbonate units, collectively called the Seroe Domi Formation, across Bonaire (Fig. 1a) and its neighbouring islands, Aruba and Curaçao. Continued tectonic activity along the Caribbean–South American plate boundary has caused uplift of the island of Bonaire, resulting in progradation and subsequent exposure of the Seroe Domi Formation, as well as younger Pleistocene carbonate successions comprised of reefal platforms (Alexander 1961; Bandoian & Murray 1974; de Buissonjé 1974; Laya *et al.* 2018). Today, a significant majority of the island is covered by these carbonate units (Fig. 1a) with isolated outcrops of older conglomerates and volcanic rocks (Westermann & Zonneveld 1956; de Buissonjé 1974). At the southern end of Bonaire, active sedimentation is taking place in the hypersaline lagoon of Pekelmeer and in the bioclastic embayment called Lac Bay (Fig. 1a; Deffeyes *et al.* 1964; Lucia 1968).

3 GPR METHOD

3.1 Background

GPR is an active-source geophysical method in which a pulsed electromagnetic (EM) wave is radiated from a transmitting antenna

(TX) and propagates through the subsurface. Some of the propagating energy is reflected at interfaces characterized by a contrast in EM impedance $Z = \sqrt{\mu/\epsilon}$, where μ is the absolute magnetic susceptibility and ϵ is the absolute dielectric permittivity. The absolute permittivity can be written as $\epsilon = \epsilon_0 \epsilon_r$ where ϵ_0 is the permittivity of free space and ϵ_r is the relative permittivity of the subsurface materials. The amount of energy that is reflected is proportional to the contrast in $\sqrt{\epsilon}$ across the interface (Davis & Annan 1989). As the reflected energy propagates back towards the surface, a small fraction of it arriving at a receiving antenna (RX) is recorded. The reflected energy is stored as a digital signal trace indicating induced RX-voltage versus time. Side-by-side layout of such digital signal traces collected along a profile displays the GPR response of the subsurface. For a more comprehensive review of EM waves, the reader is directed to Griffiths (1999), while Annan (2009) provides a detailed description of the GPR method.

The spatial resolution of a GPR survey depends on many factors but especially the frequency content of the radiated signal, with higher frequencies generally offering finer resolution (Annan 2003). The depth of investigation is also related to operating frequency (Smith & Jol 1995), and the electrical properties of the subsurface (Davis & Annan 1989). The attenuation α (dB m⁻¹),

$$\alpha = \omega \left[\frac{\epsilon \mu}{2} \left(\sqrt{1 + \left(\frac{\sigma}{\epsilon \omega} \right)^2} - 1 \right) \right]^{1/2}, \quad (1)$$

where ω is angular frequency and σ is electrical conductivity, describes the amplitude loss of an EM plane wave (Griffiths 1999). This plane wave is a good representation of the spatial component of a GPR signal at sufficiently large range. Attenuation is approximately proportional to both frequency and conductivity (Annan 1973; Bradford 2007). The inverse of attenuation is skin-depth, δ , the depth at which the amplitude of a propagating plane EM wave has decreased by a factor of $1/e$ (where e is Euler's constant, i.e. ~ 2.718), from its value at the surface (Reynolds 1997).

Limestones, such as those found on Bonaire, are relatively poor conductors with $\sigma = 5 \times 10^{-4}$ – 0.002 S m⁻¹ whereas clays are good conductors with $\sigma = 0.002$ – 1 S m⁻¹ (Davis & Annan 1989). Using these values, skin-depths can be computed for GPR signals at 100 MHz, assigning $\mu = \mu_0$, along with $\epsilon_r = 4$ – 8 for limestone and $\epsilon_r = 4$ – 50 for clay (Davis & Annan 1989). For these ranges of conductivity and relative permittivity, the geometric mean for skin-depth in limestones is 13 m, while for clays it is only 0.6 m. Thus, limestones cause less attenuation of GPR signals than clays, resulting in deeper signal penetration. Furthermore, arid conditions, such as those of Bonaire, ensure that pore-water content of rocks is low. GPR signals are attenuated in the presence of water-dissolved ions, mainly salts, since they increase bulk electrical conductivity (Annan 1996). Low water content further mitigates the effects of attenuation due to pore-water salinity during GPR acquisition.

3.2 Cross-island transect survey

The cross-island transect (CIT), completed between 2015 July 25 and August 1, was performed along a 3900-m segment of a bike trail that spans nearly the entire width of the island (Fig. 1a). The location of the CIT-enabled subsurface imaging of both leeward and windward portions of the Seroe Domi Formation since it crosses both. Common-offset acquisition was utilized during the survey. This technique maintains the TX and RX antennas at a fixed distance apart and records a single trace at each station along the transect

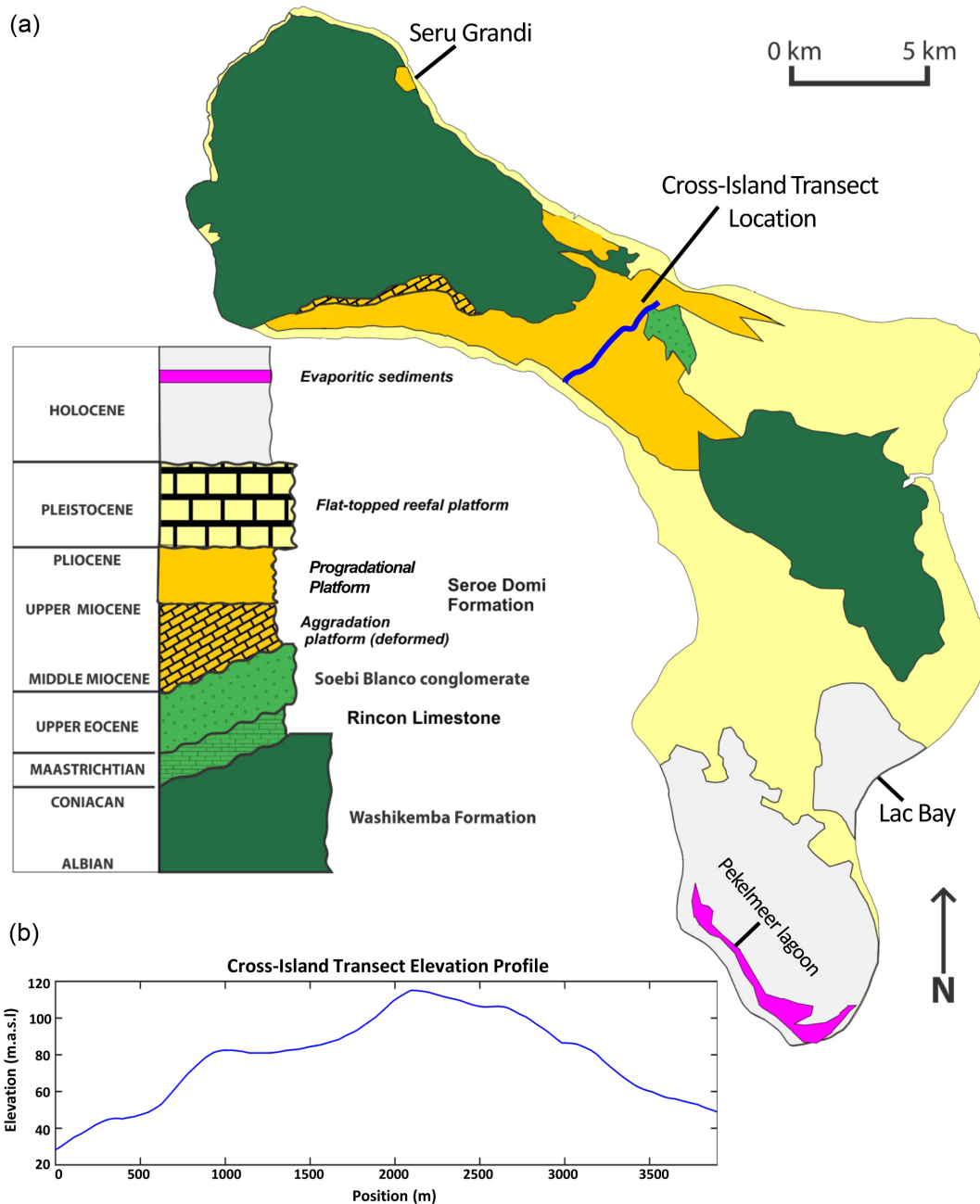


Figure 1. Map of Bonaire. (a) Generalized geologic map of Bonaire, modified after Laya *et al.* (2018). Blue line indicates location of survey site. (b) Elevation profile of cross-island transect. Elevations derived from Shuttle Radar Topography Mission data (Farr *et al.* 2007).

(Annan 2003). The signal-to-noise (SNR) ratio can be increased in this acquisition mode through stacking of traces. The survey was completed using the PulseEKKO PRO GPR system from Sensors and Software using 100 MHz bistatic antennas and a 1000 V transmitter unit. The TX-RX antenna offset was 1 m with a trace (station) spacing of 20 cm along the transect. A signal sampling interval of 0.4 ns per sample was used with a trace-window of 600 ns two-way traveltime. A stack number of 16 was chosen to improve the SNR while keeping the total acquisition time to an acceptable level. Absolute position information was sparsely collected along the CIT using a GPS unit, and was combined with satellite imagery of the bike trail region to extract a topographic profile for the CIT from the

Shuttle Radar Topography Mission (SRTM; Farr *et al.* 2007) data set (1 arc s, ~30 m lateral resolution).

4 DATA PROCESSING

Processing of the GPR data followed the steps (1–8) outlined below. Some of the processing techniques were implemented in code written specifically for this study by the first author using MATLAB, while others, where mentioned, utilize the commercial package EKKO.Project (Sensors & Software Inc. 2016). The processing workflow was as follows (Table 1):

Table 1. Outline of GPR data processing workflow, including processing parameters.

Step	Process	Parameters
(1)	Segment concatenation ^a	N/A
(2)	First-break alignment ^b	Threshold set to 5 per cent of maximum amplitude
(3)	Time-zero to first-break crop ^b	$t = 0$ ns to first-break
(4)	De-wow ^b	Filter length set to $1.33 \times$ pulse width
(5)	Background subtraction ^b	Filter shape: Nuttall-defined Blackman Harris Window Filter width: 250 traces = 50 m
(6)	Frequency filtering ^b	Low-cut: 15 MHz Low-pass: 45 Hz High-pass: 155 MHz High-cut: 185 MHz
(7)	Kirchhoff topographic migration ^a	Migration velocity: 0.1 m ns^{-1} Topographic data: SRTM ^c derived
(8)	Power-law gain ^a	Gain function: $g(t) = \alpha t^\beta + 1$ $\alpha = 1, \beta = 2$, time-window = 0–300 ns
	AGC gain ^a	AGC window = 7 samples, maximum scalar gain = 100, time window = 0–300 ns

^aMATLAB implementation.

^bEKKO_Project routine (Sensors & Software Inc. 2016).

^cShuttle Radar Topography Mission (Farr *et al.* 2007).

(1) Segment concatenation was first applied to merge into one contiguous file the entire GPR profile that was originally collected in segments defined by pauses in acquisition.

(2) First-break alignment (Cassidy 2009) was then applied to automatically detect the onset of recorded EM energy for all traces and individually shift them in time to correspond with a reference time. This operation was applied using the EKKO_Project software, and corrects for instrument timing issues and the effect of small terrain irregularities on antenna placement.

(3) The delay between time-zero (the time at which the RX begins recording) and the first-break was then muted and time-zero reassigned to the first-break time. This delay corresponds to the traveltimes of the direct wave from the TX to the RX. With the assumption of a constant subsurface EM wave velocity, the removal of this delay accounts for the offset between the TX and RX, effectively creating a zero-offset section, although it does not remove the ubiquitous ground-clutter.

(4) Using the EKKO_Project software, the data were ‘de-wow’d’. This step removes the low-frequency bias in each of the traces due to either inductive coupling of the TX–RX (Annan, 2003, 2009) or amplitude saturation of the electronics by the direct wave (Gerlitz *et al.* 1993).

(5) A lateral (across-trace) moving weighted-average was then used as a background subtraction filter (Table 1). This filter removes the high-amplitude direct wave that can mask early-time reflections, and also reduces the effects of antenna ringing (Everett 2013).

(6) Frequency filtering was then performed to mitigate recorded signals occurring outside the -3 dB roll-off defining the bandwidth (50–150 MHz) of the antennas used in this study. An appropriate bandpass filter was designed using EKKO_Project (Table 1).

(7) A topographic Kirchhoff migration (Dujardin & Bano 2013) was implemented for the purpose of collapsing diffraction hyperbolae and restoring dipping reflections to their true spatial locations (Claerbout 1985; Yilmaz 2001). The benefit of topographic migration is that the relative vertical position of the GPR acquisition system is taken into account without the need for a separate topographic correction step. Moreover, as relative elevation changes along the GPR transects are on the same scale as the depths of investigation, topographic migration provides more accurate imaging than topographic correction, followed by a fixed-datum migration (Lehmann *et al.* 1998; Dujardin & Bano 2013). The STRM-derived

elevation profile of the CIT was interpolated to the 0.2 m GPR trace spacing and provided as an input to the topographic migration algorithm.

Previous studies utilizing GPR in limestone lithologies have shown insignificant variation in average velocity with depth (Forte *et al.* 2012; Menezes *et al.* 2016) and little improvement to imaging from using more complex velocity models. Therefore, iterative constant velocity migration attempts were made at multiple locations along the CIT (one example test location is shown in Fig. 2). During visual inspection of these migration test results, a constant 0.1 m ns^{-1} velocity model consistently proved to best collapse observed diffraction hyperbolae at each test location. (Figs 2c and d).

(8) Gain was applied to the GPR lines to compensate for geometrical spreading (Yilmaz 2001) and other forms of attenuation. Two gain functions were applied independently (not consecutively) to the data. The first was a t^2 power-law gain (Claerbout 1985) wherein amplitudes are scaled according to the square of their traveltimes. This gain compensates for the effects of geometrical spreading while retaining the relative amplitude, both along a given trace and between traces. The second gain was an Automatic Gain Control (AGC) function that seeks to gain each recorded sample based on the average amplitude of a surrounding window compared to the maximum amplitude occurring in the ungained trace. The benefit of the AGC gain is to normalize the amplitudes of reflections within the gain application window. This improves the continuity of reflections and facilitates structural interpretation. However, the relative amplitude information of the data is not preserved in the AGC process. To avoid overamplification of signals below the noise threshold, a maximum allowable gain was set when applying the AGC. Both the attenuation and AGC gains were not applied beyond 300 ns in each trace to avoid amplification of artefacts below the depth of investigation.

5 SEMI-AUTOMATIC CLASSIFICATION OF GPR DATA

The CIT survey spanned 3900 m with traces every 20 cm, giving 19 500 traces. With each trace in the data set consisting of 1500 samples, the entire CIT contains over 29 million individual amplitude measurements. It is advantageous to interpret such a

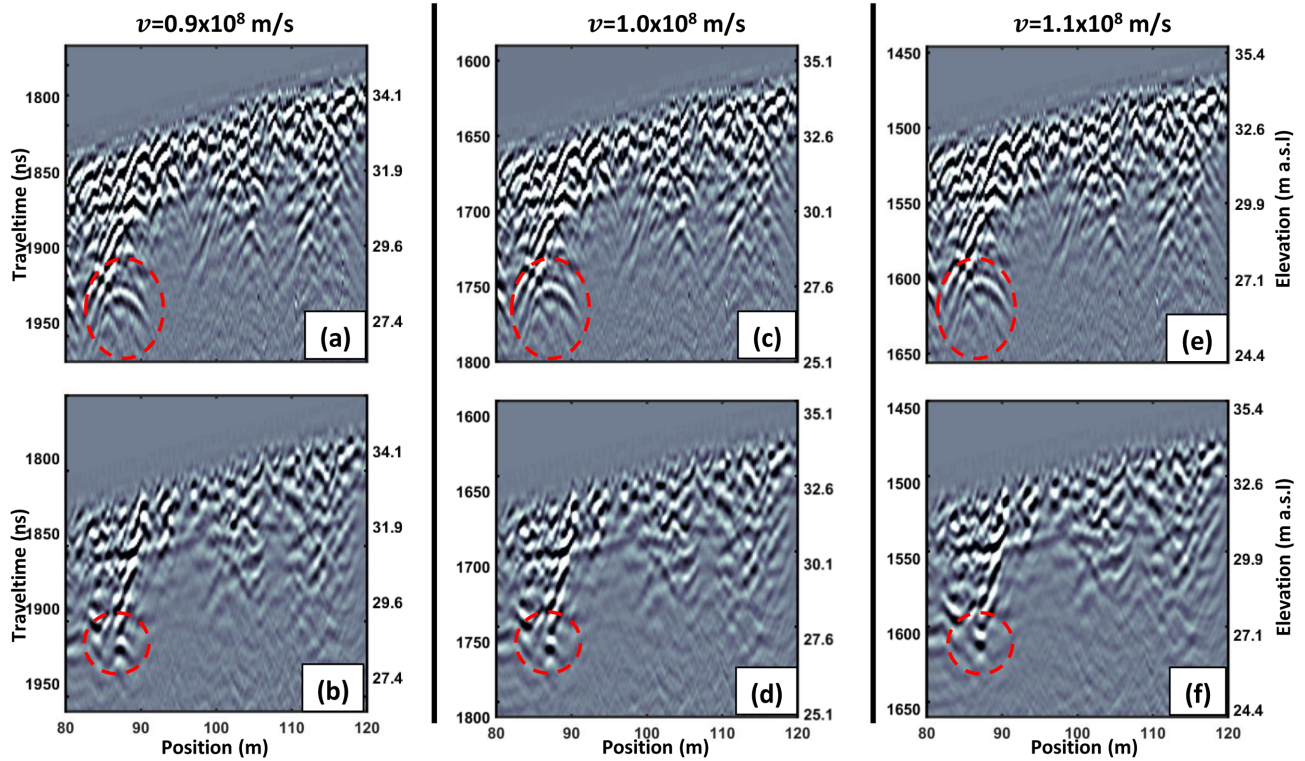


Figure 2. Topographic correction but no migration (top panels) versus topographic migration (bottom panels) at $x = 80\text{--}120$ m along CIT. (a and b) $v = 0.9 \times 10^8$ m s⁻¹, (c and d) $v = 1.0 \times 10^8$ m s⁻¹ and (e and f) $v = 1.1 \times 10^8$ m s⁻¹. Ovals indicate diffractions of interest. Power-law gain applied to all radargrams.

high resolution data set efficiently while, at the same time, maintaining objectivity and consistency. Traditional manual methods of observation and interpretation provide a subjective, and often time consuming approach to identification of features such as radar facies (Neal 2004) and individual geologic structures. To increase the confidence in interpretation along the CIT, and to provide a more quantitative approach to interpretation, a method of k -means clustering of structure-parallel vectors was developed. This method automatically segments a GPR image based on the local orientation of reflections.

5.1 k -means clustering of structure parallel vectors

In its simplest form, k -means is a method for organizing a set of N vectors into k groups. This process was discussed by MacQueen (1967) as a method for partitioning data into groups that have low within-group variance and consequently higher intragroup variance. The k -means algorithm compares each vector comprising a data set to the average, or mean, values of non-overlapping subsets of data belonging to a specified number of clusters. A more detailed description of the traditional k -means algorithm (after Steinley 2006) is provided in the Appendix.

In clustering of images, each vector in the data set usually corresponds to an attribute of an individual pixel in the image. Popular definitions for these vectors are pixel colour, measures of intensity or texture (Jain *et al.* 1999; Jain 2010). Instead of such metrics, the method implemented for this study utilizes neighborhoods of structure-parallel vectors (Hale 2009), associated with each pixel in a GPR image (see the Appendix).

A structure-parallel vector is derived from an image structure tensor (Hale 2009) that is the smoothed outer product ($\nabla u \nabla u^T$)

of the image gradient ($\nabla u(x, y)$) with itself (Van Vliet & Verbeek 1995; Weickert 1995; Fehmers & Höcker 2003; Hale 2009). For GPR images, $u(x, y)$ is the amplitude of the individual pixel at location (x, y) . In this study, image gradients were computed using Gaussian derivative filters with radii $\sigma = 1$ pixel and outer products were smoothed using Gaussian smoothing filters with radii $\sigma = 10$ pixels (with the spatial scale of 1 pixel in the CIT GPR image being 0.2×0.02 m). The size of the smoothing radius was chosen in order to eliminate the influence of fine-scale irregularities in the image while preserving geometries representative of geologic structures (Bowling 2017).

Computation of a structure-parallel vector begins with the eigen-decomposition of a structure tensor S ,

$$S = \lambda_u \mathbf{u}\mathbf{u}^T + \lambda_v \mathbf{v}\mathbf{v}^T, \quad (2)$$

where \mathbf{u} and \mathbf{v} are the eigenvectors and λ_u and λ_v are the eigenvalues defined with $\lambda_u \geq \lambda_v \geq 0$ (Hale 2009). It can be shown that the eigenvectors of S are orthonormal ($\mathbf{u}^T \mathbf{u} = \mathbf{v}^T \mathbf{v} = 1$; Weickert 1995) with \mathbf{u} pointing in the direction of maximum image gradient and \mathbf{v} pointing in the direction of minimum image gradient (Van Vliet & Verbeek 1995; Hale 2009).

For GPR images, gradients in signal amplitude are generally highest in the direction perpendicular to reflections within the image and lowest paralleling reflections. Given that these reflections define the structural geometries of the image (and potentially the geology of interest), for a structure tensor S , the eigenvector \mathbf{v} can be described as a *structure-parallel* vector with \mathbf{u} being a *structure-perpendicular* vector. An example of a subset of structure-parallel vectors computed from a portion of the CIT is shown in Fig. 3(a).

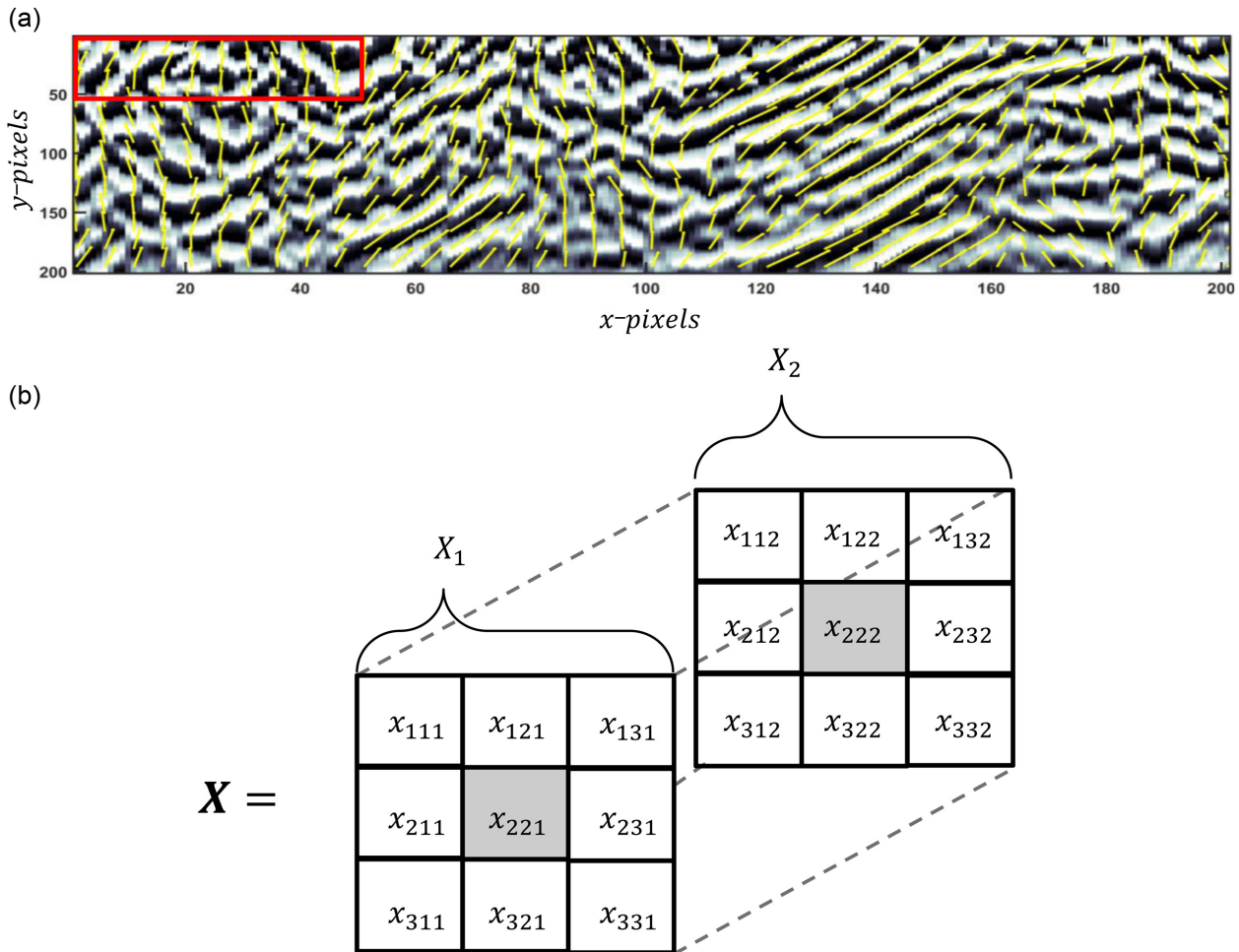


Figure 3. (a) A subset of structure-parallel vectors (every fourth in x and every eighth in y) overlain atop a portion of the CIT survey. Axes are labelled in pixels. Red box indicates size of 51×51 vector patch. (b) Visual diagram of an example 3×3 patch of structure-parallel vectors, \mathbf{X} , centred on vector x_{221} indicated by grey box.

The lengths of all structure-parallel vectors computed in this study have been scaled by the linearity, λ_1 , of the associated structure tensor. Using the notation after Hale (2009), the linearity is defined as

$$\lambda_1(x, y) = (\lambda_u - \lambda_v / \lambda_u). \quad (3)$$

Orientations described by structure tensors with high linearities are comparatively more consistent (Van Vliet & Verbeek 1995), and well defined. In a GPR image, higher linearities correspond to sharper reflections, and the scaling of structure-parallel vectors by linearity serves to emphasize such features in the clustering.

A structure-parallel vector computed from amplitudes at a given GPR image point describes the linear orientation of a reflection averaged over the radius of smoothing (here 10 pixels). Yet geologic features that are of interest to this study, such as clinoforms, karstic features, gradational changes in dipping beds, etc., may contain multiple orientations over their spatial extent. Therefore, instead of performing k -means clustering through observation of each individual vector in the structure-parallel vector field, instead patches of vectors are compared (see the Appendix; Fig. 3b). A patch size of 51×51 structure-parallel vectors (approximately 1×10 m in vertical and horizontal extent, respectively) was selected for use as the basis of clustering the CIT. This patch size allowed for features at the scale of interest in this study to be compared, while features at

significantly smaller scales than the patch (red rectangle in Fig. 3a) were given less importance in the clustering (Bowling 2017).

In this method, the number of clusters, k , chosen in the k -means algorithm serves as a way to choose how distinct individual clusters are from each other (Bowling 2017). For clustering performed on the CIT, a choice of $k = 8$ allowed for the best trade-off between detailed identification of features and structurally distinct clusters.

In any k -means method, initial cluster means must be chosen (Steinley 2006). In this work, initial cluster means were manually chosen to correspond with regions in the CIT that appear to be structurally different from one another. The use of user-defined means prevented overdetermination of clusters (Bowling 2017), and allowed for prior knowledge of significant features in the image to be included in the clustering.

5.2 CIT clustering results

Using the methodology outlined above and described in the Appendix, k -means clustering of structure-parallel vectors was performed on the full CIT (Fig. 4). Given that structure-parallel vectors are sensitive to local changes in gradient, relative amplitude changes along a reflector will affect their orientation. However, when the GPR data are AGC gained, relative amplitudes are removed and only the structural aspects of the reflections remain.

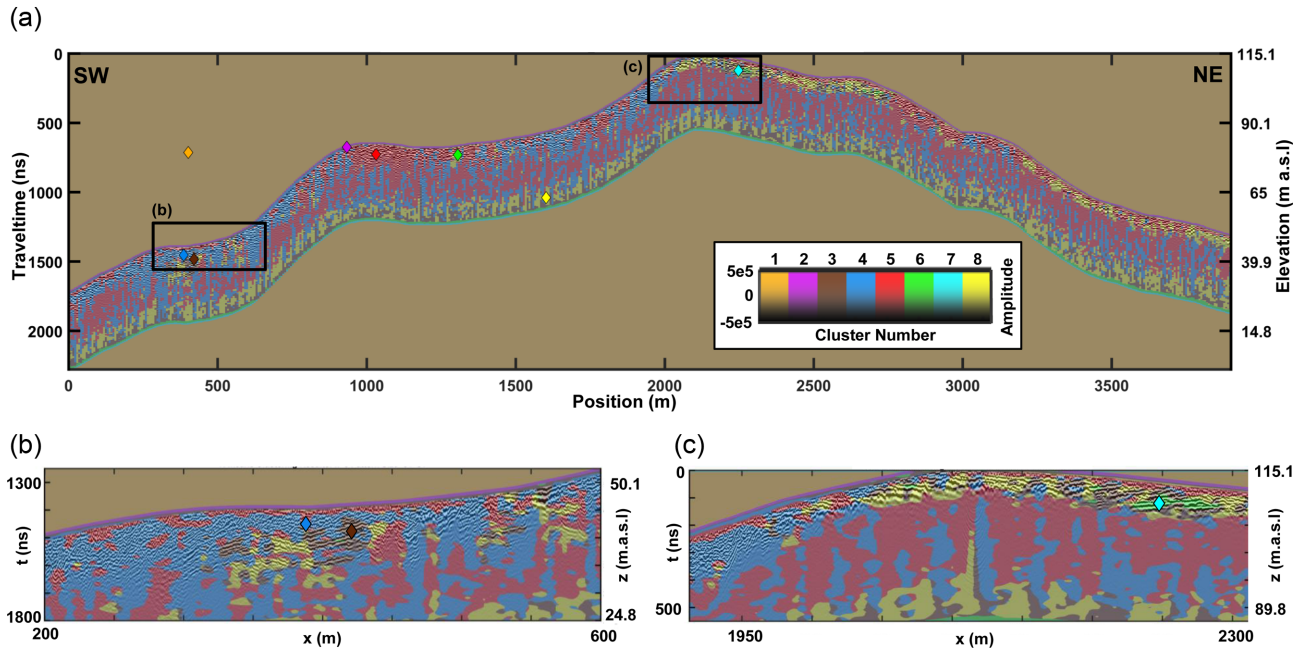


Figure 4. Results of *k*-means clustering of structure-parallel vectors applied to the CIT. (a) Full CIT with clustering results semi-transparently overlain on AGC-gained radar amplitudes. Coloured diamonds represent locations where initial means were chosen. (b) Close up of clustering results for $x = 200\text{--}600$ m. (c) Close up of clustering results for $x = 1912.6\text{--}2312.6$.

Therefore, clustering in this study was performed after application of AGC to the CIT. This choice simplified further analysis as interpretations of the clustering are not influenced by relative amplitude information. To quantify the orientations of vectors classified into each cluster, dip-histograms were created. These plots (Figs 5a–h) show that for each cluster, the number of structure-parallel vectors falling within a bin represent a given range of dips. The dips in these histograms represent actual apparent dips as the length of each vector component was converted from pixels to metres prior to the dip calculation. In addition to binning the vectors by dip, each bin was then colour-coded according to the average linearity of the vectors in that bin. Recall that each structure-parallel vector was scaled by the linearity parameter, λ_1 , which ranges from 0 to 1. Vectors with larger associated values of linearity describe features that produce larger image gradients and therefore define regions with more distinct local orientations.

The results of the *k*-means algorithm show that clusters 1, 2 and 7 classify regions in the image that are not associated specifically with GPR reflections. Cluster 1 classifies the zero amplitude regions in the image that bound the GPR data. Clusters 2 and 7 classify the upper and lower edges of the GPR traces, respectively. Each of these clusters contains vectors that largely have zero dips and zero values of linearity (Figs 5a, b and g). This indicates that the features associated with these clusters either produce no image gradients (as in the case of cluster 1) or transition from high-gradients to zero gradients (clusters 2 and 7).

The remaining clusters (3–6 and 8) each identify features associated with structural aspects of the GPR reflections in the CIT. Cluster 3 classifies relatively low-angle, southwest dipping reflections in the CIT with structure-parallel vector dips between 5° and 90° (Fig. 5c). Cluster 4 contains reflectors that are more steeply dipping to the southwest than those in cluster 3. The dip histogram in Fig. 5(d) for this cluster shows that dips are distributed between 20° and 60° . Cluster 5 identifies reflections that are dipping steeply to the northeast. The vectors in cluster 5 have dips falling between

20° and 60° . Although these dips generally mirror the range of dips defined by cluster 4, the dip distribution of cluster 5 is broader and encompasses dips that are up to 90° . Furthermore, cluster 5 shows a bimodal distribution for vectors with high linearities (Fig. 5e). Cluster 6 classifies GPR reflections that are near-horizontal compared to surrounding reflections. The dip-histogram for cluster 6 (Fig. 5f) shows that the majority of the vectors in this cluster have dips less than 10° . Cluster 8 contains vectors associated with comparatively low-angle northeast dipping reflections. Cluster 8 shows the narrowest distribution of vector dips for any cluster within the CIT, with the majority of dips ranging from $10^\circ\text{--}35^\circ$ (Fig. 5h).

The linearity values can be seen to vary significantly between the clusters (Fig. 5). Clusters 4 and 5 have a larger proportion of their vectors with high linearities ($\lambda_1 \geq 0.87$), as compared to clusters 3, 6 and 8. This indicates that features associated with clusters 4 and 5 produce high gradients, meaning they contain sharp, clear reflections, in the CIT. Reflections associated with these two clusters are higher in frequency compared to reflections associated with clusters 3, 6 and 8 (Fig. 6). The broader wavelets of the low-frequency reflections result in the lower linearities associated with vectors in clusters 3, 6 and 8 versus clusters 4 and 5.

It is important to note that many of the vectors within cluster 6 have very low linearities compared to the other clusters (rarely exceeding $\lambda_1 = 0.74$). This is likely due to the fact that the majority of vectors in this cluster are found near the bottom edge of the GPR data, with few residing within the GPR reflections themselves. At the bottom of the data, the low-amplitude migration artefacts characterized by very broad semi-ellipse shapes exhibit near-horizontal orientations and consequently are classified by cluster 6. Despite much of cluster 6 identifying these migration artefacts, there exists several regions within the GPR reflections where actual horizontal reflections are well classified by cluster 6 (Figs 4c and 6), therefore making this cluster important when considering geologic interpretation of the CIT.

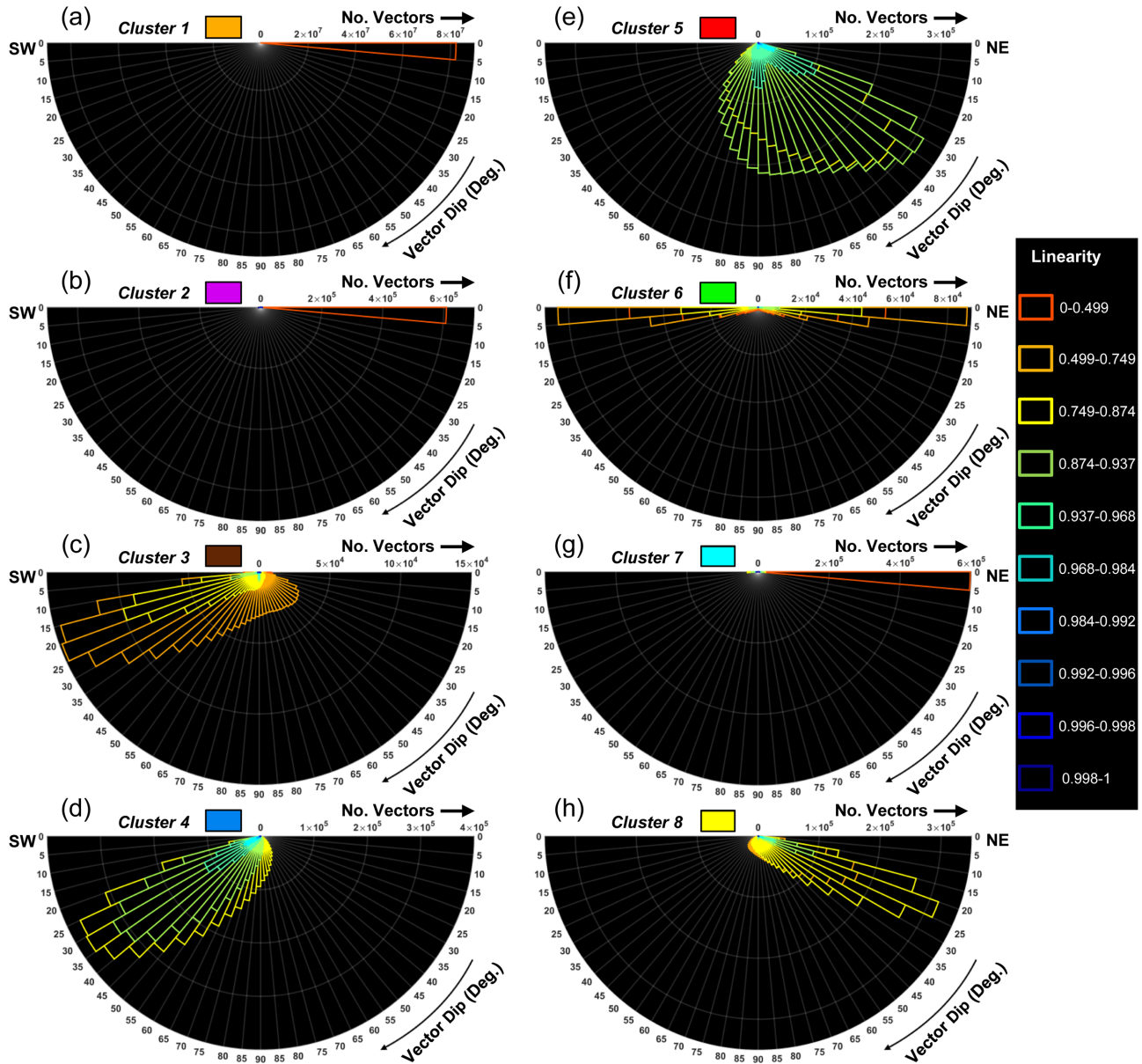


Figure 5. Dip histograms for each cluster, indicating vector dips and average linearity by 5° bins. (a-h) Dip histograms for clusters 1–8, respectively.

Many of the clustering results are intuitive when considering the initial mean assignments for the clusters (Fig. 4). However, some non-intuitive results exist. The final assignments of cluster 7 may appear surprising when considering the initial mean for cluster 7 was chosen in a region with well-defined GPR reflections (Fig. 4c). We observed that the relatively flat-lying reflections at the location of the initial mean for cluster 7 produced structure-parallel vectors that were similar to those produced at the location of the initial mean chosen for cluster 6 (broad semi-ellipse shapes). With two similarly initialized means, the k -means algorithm began by attributing such features to either cluster before successive iterations better differentiated the two groups. This observation illustrates that while the results of k -means clustering of structure parallel vectors is influenced by the initial means, the relative influence of the actual proportions of features in the image ultimately determines which regions in the image will be associated with what clusters (Bowling 2017).

5.3 CIT radar facies derived from clustering results

From the results of the k -means clustering, the clusters (3, 4, 5, 6 and 8) that are associated with the informative parts of the GPR image, that is, radar reflections, were used to describe a set of radar facies (Neal 2004). However, each individual cluster does not fully describe a unique radar facies. The clusters have been shown to identify reflections that fall within a specific range of orientations, yet geologic structures as described by radar facies may contain multiple orientations over their extent. Therefore, combinations of clustering assignments were considered when determining radar facies. Moreover, the clustering assignments do not take into account reflector amplitude. Using the CIT with the application of the power-law gain as described in section 4, relative amplitude variations along reflections aided in determining radar facies. With these considerations, six radar facies (R1–R6) were identified within the CIT. Descriptions of the various facies include information about reflection dip, amplitude, shape and relationships between reflections.



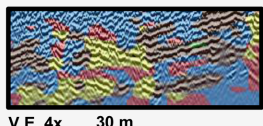
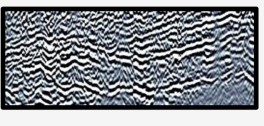



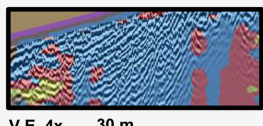
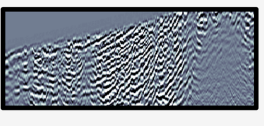


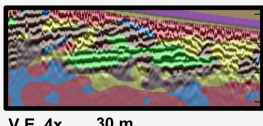
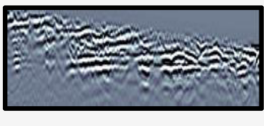



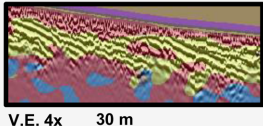
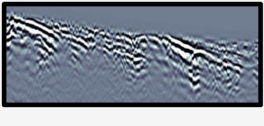



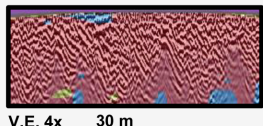
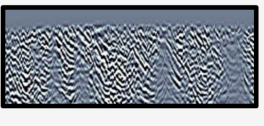
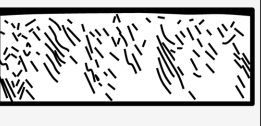

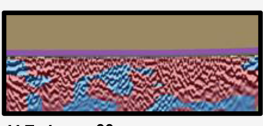
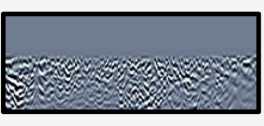
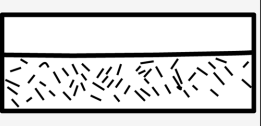
Facies	Description	Primary Clusters	Associated Clusters	Example (Clustering, Relative Amplitudes, and Line Drawing)		
R1	Parallel to sub-parallel hummocky reflectors with high amplitudes. Generally continuous with dips 0-15° to SW.	3, 4 and 8 	5 	 V.E. 4x 30 m		
R2	High angle (20-40° to SW), narrow, subparallel to divergent reflections. High amplitude. Sometimes with lower amplitudes and less continuity.	4 	5 	 V.E. 4x 30 m		
R3	Near-horizontal (0-15°) parallel to subparallel reflections. Generally very high amplitude and laterally continuous.	3, 6 and 8 	None	 V.E. 4x 30 m		
R4	Sigmoidal and subparallel reflections, having very high amplitudes. Sometimes showing offlap patterns. Generally Continuous with dips 10-25° to NE.	8 and 5 	3 	 V.E. 4x 30 m		
R5	High angle (25-45° to NE), frequently discontinuous, with moderate amplitudes. Local regions display more chaotic shapes.	5 	4 	 V.E. 4x 30 m		
R6	Highly discontinuous high angle (>45°) reflections. Parallel to subparallel at very local scales, bordering on chaotic. Typically have low to moderate amplitudes	4 and 5 	None	 V.E. 4x 30 m		

Figure 6. Radar facies summary with descriptions of each of the six radar facies identified in the CIT along with the clusters that define the geometries of the facies. Examples are shown for the clustering results, power-law gained radar amplitudes and resulting line-drawing for each of the radar facies types.

Reflection shape and relationships between reflections are described using terminology from seismic stratigraphic analysis (Mitchum Jr *et al.* 1977; Vail 1987). Each of the radar facies is described in detail below, and a summary of these descriptions, along with examples of each facies is shown in Fig. 6.

R1—The reflections in this radar facies are typically parallel to subparallel with largely shallow dips to the southwest and often contain small-scale hummocky irregularities. The more continuous reflections in this facies are generally low frequency and have high amplitude. R1 is primarily characterized by clusters 3, 4 and 8. Reflections with low-angle (<10 degrees) southwest dips are classified by cluster 3, areas of flat to northeast dips are classified by cluster 8 and the more complex areas with locally steep dips are classified by cluster 4. Within these, small patches of complex reflections showing steep northeast dips are classified by cluster 5. Cluster 5 is deemed a subordinate or ‘associated’ cluster because it often occurs within the radar facies as a minor constituent of isolated features.

R2—This facies contain narrow, mostly subparallel to oblique, high amplitude reflections that are steeply dipping to the southwest. From the *k*-means clustering results, the more continuous reflectors in R2 are classified by cluster 4. Small patches of discontinuous reflections with southwest dips classified by cluster 5 also exist within this facies. These more complex regions have comparatively

lower amplitudes than the more continuous reflections in this radar facies.

R3—This radar facies is composed of generally parallel to subparallel, high-amplitude, horizontal to subhorizontal reflections. As the dips for this facies are near horizontal, classification by clusters 3, 6 and 8 occurs as each of these clusters classifies horizontal or near-horizontal dips. Reflections in R3 are broader in width than surrounding reflections.

R4—Radar facies R4 consists of laterally continuous, very high amplitude reflections that dip gently to the northeast. These reflectors typically exhibit sigmoidal to subparallel patterns, with some reflections showing progradational patterns. This facies is mainly classified by cluster 8 from the *k*-means clustering, yet where reflectors in this facies are nearly flat lying or dipping slightly southwest, these portions are classified by cluster 3, and where reflections become more discontinuous and complex, these areas are classified by cluster 5.

R5—This radar facies characterizes reflections that are generally moderate in amplitude that often dip steeply to the northeast. Features in R5 are significantly more discontinuous than other radar facies, and include a larger fraction of complex regions. Most of the reflections in R5 are classified by cluster 5. Although, similar to R2, isolated patches of low-amplitude reflectors with opposing,

southwesterly, dips classified by cluster 4 also occur within this facies.

R6—This facies describes highly discontinuous groups of reflectors of low-to-moderate amplitude having very-high-angle dips. Reflections are either classified by cluster 4 or 5 depending on whether dips are oriented, respectively, towards the southwest or northeast. Reflections in this facies are parallel to subparallel at scales of less than 5 m, but appear chaotically organized at larger scales.

6 DISCUSSION

6.1 Strata geometries

Each of the six radar facies was mapped in detail along the CIT, revealing the strata geometries of the Seroe Domi Formation. A detailed example of these geometries is shown in Fig. 7 for representative portions of radar facies R3 and R4, where the relative amplitude information of the GPR transect as well as the clustering results are compared to the facies mapping. A generalized radar facies mapping across the entire CIT is shown in Fig. 8. This cross-section summarizes the information derived from the interpreted radar facies, and also includes locations and corresponding lithologies of hand-drilled core samples previously collected along the Bonaire bike trail (Sulaica 2015). Fig. 8 shows significant contrasts in stratigraphic geometries between the windward and leeward sides of the CIT, which are described herein.

In the southwest portion between 200 and 800 m, transitions between R1 and R2 are mapped. The low-angle parallel to subparallel orientations of reflections in R1 suggests sediments deposited in original depositional orientation with a flat foreshore position. Here, environments would have been relatively low-energy, such as those dominated by subtidal forces within the protected area of the leeward side of the island (Tucker & Wright 1990; Lucia 2007; James & Jones 2016). These types of low-energy environments are associated with increasing carbonate muds in portions of progradational platform units (Laya *et al.* 2017) and may be the source of the R1 radar reflections. In contrast, the higher angle of the reflections in R2 compared to R1 implies that sediments may have been deposited in areas of relative higher energy, such as foreshore slopes that were subject to mild wave action (Tucker & Wright 1990; Pomar *et al.* 2015; James & Jones 2016). Radar patterns analogous to R2 were observed by Jorry & Bièvre (2011), which were there linked to units of bioclastic packstone/grainstones indicating higher relative energy environments. The alternating packages of R1 and R2 may represent depositional responses to sea-level fluctuations, thus creating transitions between shoreface and subtidal deposits that are preserved on the protected leeward side. Similar radar facies associations are also seen at ~1600 m in Fig. 8, indicating that multiple periods of shoreface transgression and regression may be preserved on Bonaire.

At the far southeastern portion of the CIT, the higher angle reflections described by radar facies R2 (Fig. 8) are possibly caused by tectonic deformation as opposed to the higher wave energies previously discussed. The mapping of this facies at the bottom of the stratigraphy on the southeastern side of the CIT correlates with observed tectonic deformation of the lower Seroe Domi Formation (Fig. 1a), as suggested by previous workers (Hippolyte & Mann 2011; Sulacia *et al.* 2015; Laya *et al.* 2018).

At the highest portions along the bike trail (2000–2700 m; Fig. 8) multiple regions of the radar facies R3 were mapped. The low-angle reflections of this facies (Fig. 6) would initially suggest low-energy

environments of deposition. However, previous workers have described sediments with very-well-sorted bioclast fragments (green triangles in Fig. 8), mainly of benthic foraminifera (*Amphistegina sp.*), bryozoans and bivalves, and high-angle cross-bedding derived from windblown sediments (Bandoian & Murray 1974; de Buissonjé 1974; Sulaica 2015; Laya *et al.* 2018) occurring at the same locations where R3 is mapped along the CIT (Figs 7 and 8). With the estimated vertical resolution for the GPR data in the CIT being on the order of tens of cm, it is likely that individual high-angle foresets within these types of sediments are too small to be resolved. Instead, it is probable that what is being imaged are the lower-order bounding surfaces (Bristow 2009) that have much shallower dips within sediment packages (Brookfield 1977), resulting in the low-angle character of R3.

The majority of the northeastern windward portion of the CIT consists of radar facies R4. The sigmoidal reflector shapes of this facies are characteristic of clinoforms created from costal foreslope deposits (Eberli & Ginsburg 1989; Mutti *et al.* 1996; Pomar & Hallock 2008; Hazard *et al.* 2017). During the depositional stage creating these units, accommodation space would have been very limited and would have forced sediments to shed laterally, forming the geometries of R4 at the platform margin (Schlager *et al.* 1994). Occurrences of R4 along the northeastern part of the CIT are comparable to outcrop-interpreted clinoforms, which have been observed at multiple locations in the northeast part of the island [e.g. outcrop in Fig. 9 and at Seru Grandi (Laya *et al.* 2017)]. The geometries of the clinoforms observed in outcrop (yellow lines, Fig. 9e) compare well with those contained in R4. In addition, outcrops show near-vertical fractures cross-cutting clinoform traces (black lines, Fig. 9e). If similar fracture styles occur in the subsurface along the bike trail, it would account for the sometimes discontinuous nature of R4. Moreover, the northeast orientation of the clinoforms in R4 supports the idea of eastward-directed regional Caribbean tectonic movements that influence the local depositional system (Hippolyte & Mann 2011; Sulaica 2015; Laya *et al.* 2018).

Beyond the well-defined reflectors described by R1–R4, multiple locations described by the highly discontinuous reflectors of R5 or R6 were also mapped along the CIT. These discontinuous reflections have been attributed to the scattering of EM waves and complex radar returns arising from near-surface karstification caused by meteoric weathering. The complex reflections defining radar facies R6 do not appear to have any preferential orientation; therefore, we describe this facies as unstructured karst. However, the northeast orientation of many reflections in radar facies R5 do suggest a preferential orientation of karstification, possibly due to tectonic deformation (Shanov & Kostov 2015). We hereafter define these complex and discontinuous features described by R5 as structured karstification. Karstification, as observed by both R5 and R6, heavily modifies depositional structures and therefore obscures interpretation of original geometries.

A large portion of such karst was mapped at ~1000 m (Fig. 8) with the structured karstification of R5 being flanked by unstructured karst (R6). Observations of partly dolomitized rocks occurring at similar locations (Sulaica 2015; white triangles in Fig. 8) support the idea of a lagoon where perhaps denser mesohaline waters contributed to dolomitization (Laya *et al.* 2018). Such a lagoon would have allowed for the deposition of the observed low-angled strata (mapped as R4 between 1250 and 1500 m in Fig. 8) bounded by karstification associated with fossilization of costal corrosive mixing zone areas [a process suggested by Smart *et al.* (1988) and Mylroie & Carew (1995)]. Due to the tectonic uplift (Smart *et al.*

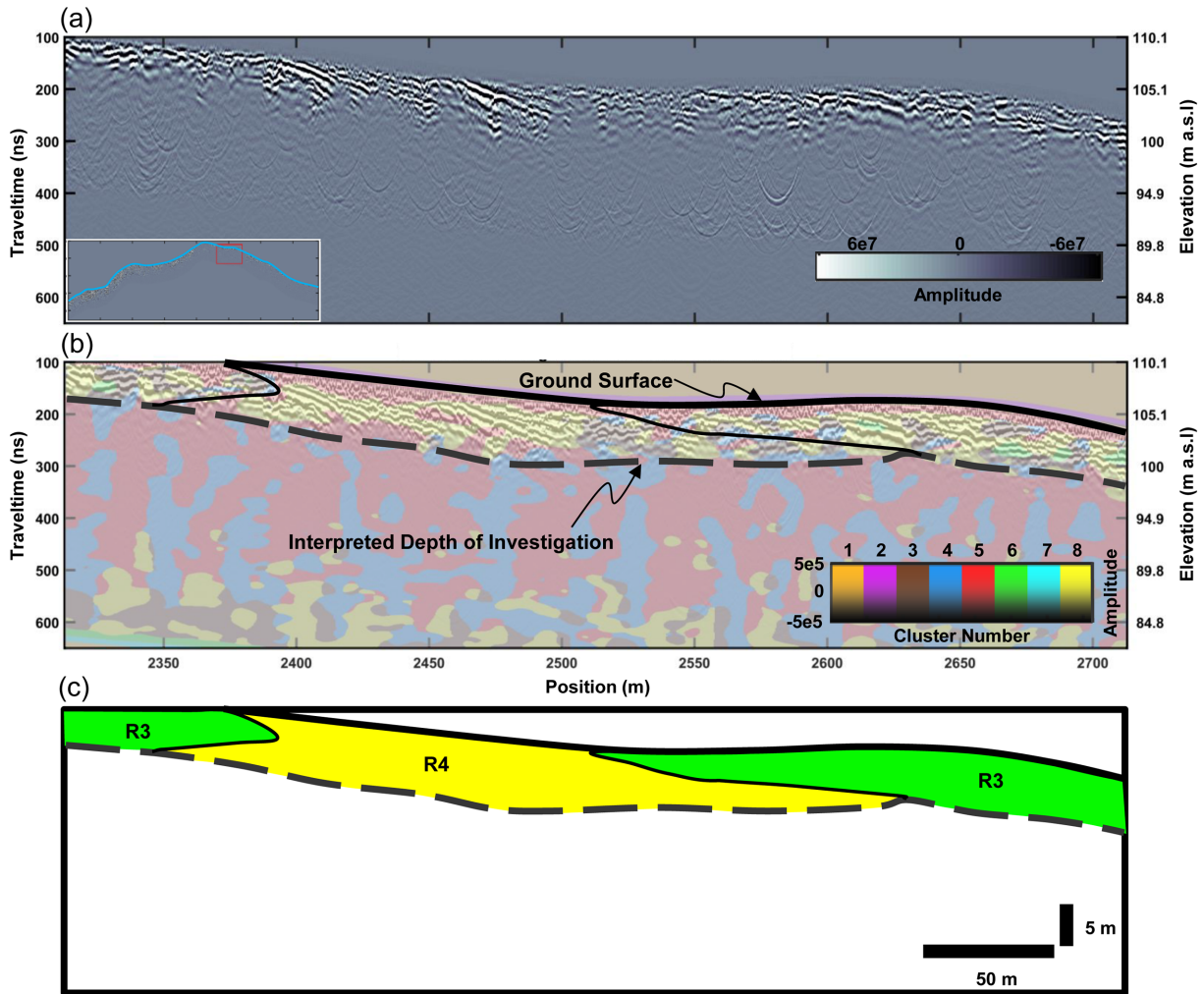


Figure 7. Radar facies mapping $x = 2312.8\text{--}2712.8$ m. (a) Power-law gained GPR section. Inset map showing location of section with respect to full CIT. (b) Clustering results with facies boundaries outlined. (c) Cross-section showing radar facies distribution.

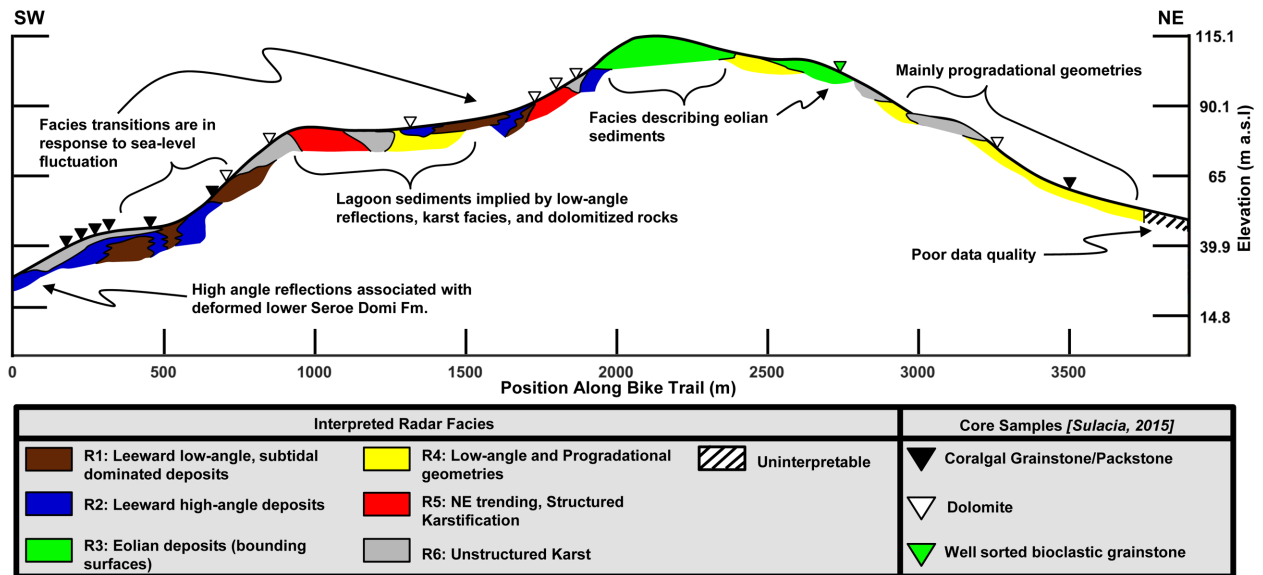


Figure 8. Radar facies mapping across CIT. Coloured triangles represent locations and lithologies of hand-drilled core samples from Sulaica (2015).

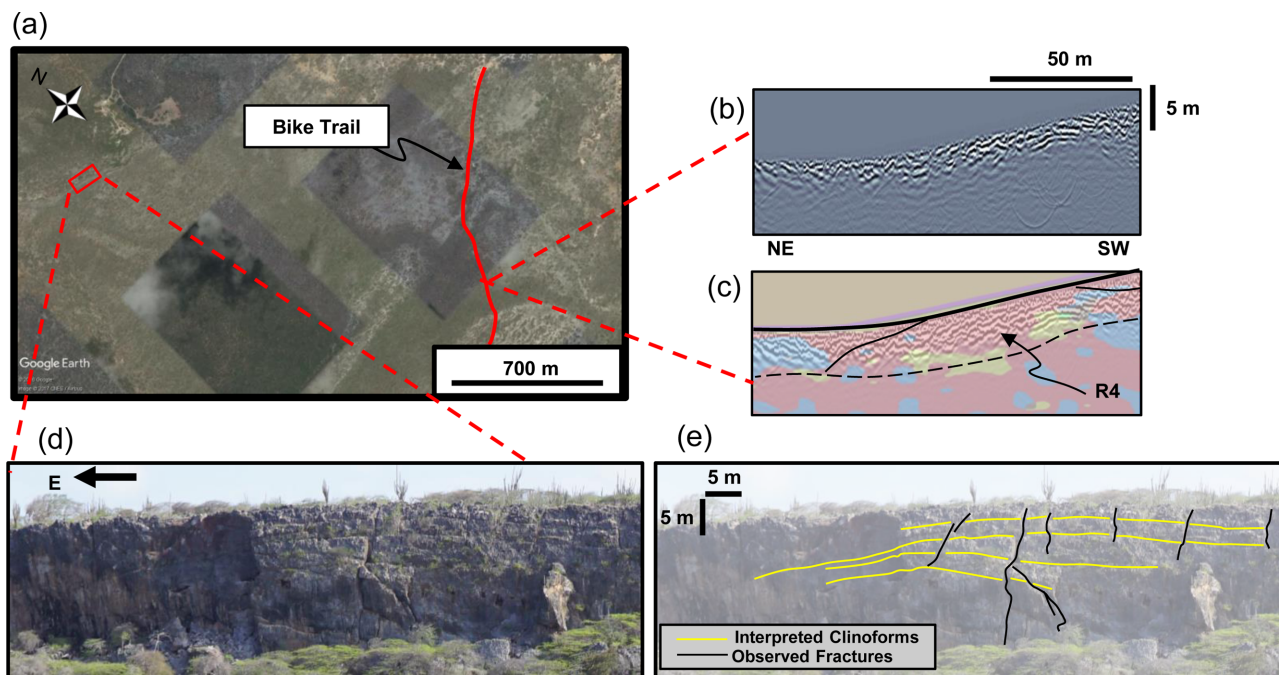


Figure 9. R4 compared to outcrop observations. (a) Satellite photo showing location of Bonaire bike trail and respective locations for GPR segment and outcrop photo. (b) GPR amplitudes along a northeast portion of the CIT. (c) Interpretation of R4 from GPR clustering results. (d) Outcrop photo at location shown in (a). (e) Interpreted clinoform geometries as well as observed fractures on outcrop photo.

1988), these once submerged structures are 55–65 m above sea level at the present day.

6.2 Implications for geologic evolution of Bonaire

The identification and interpretation of the radar facies map across the central portion of Bonaire facilitates a detailed understanding of the prograding platform within the Seroe Domi Formation. By examining these lithologies at the 1–10 m scale using GPR, we were able to identify a complex set of geometries reflecting tectonic, depositional and diagenetic events defining the geologic evolution of the island.

The initial deformation and uplifting that was responsible for tilting the lower Seroe Domi Formation (inclined beds at the western side of the island) established a basal topography (Hippolyte & Mann 2011; Laya *et al.* 2018). We observe some steeply inclined reflectors mapped as radar facies R2 that perhaps are associated with this deformation at the deepest part of the profile (~0–100 m, Fig. 8). Prograding platform units were deposited atop these inclined beds with accommodation space being controlled by the basal topography and sea-level highstand conditions (Haq *et al.* 1987; Fouke *et al.* 1996; Reijmer *et al.* 2002; Laya *et al.* 2018). This forced progradation of sediments to the east as evidenced by the occurrence of the sigmoidal clinoform reflections of R4 in the northeast portion of the CIT. Work by Laya *et al.* (2018) proposes that grainy deposits of the prograding platform (high-energy environments) are transitional to the coastal–continental deposits of the eolianites with an absence of coral reef facies in the succession. This transition is evident in the CIT, where radar facies R4 at the northeast portion of the line transitions to facies R3 in the central portion of the island.

Furthermore, multiple depositional environments are inferred on the sheltered side of the progradational platform; these are evidenced by the complexity of the radar facies occurring on the south-central portion of the CIT. As mentioned previously, radar facies and

facies associations at these locations suggest shoreface producing environments, and associated low-energy lagoonal environments, which can be linked to dolomitization.

6.3 Implications for subsurface mapping of carbonates using GPR

The utility of GPR to investigate the near-surface structural geologies across the island of Bonaire depends heavily on the site geology. As mentioned in section 3.1, the dry carbonate rocks found across the central portion of Bonaire cause less attenuation of EM waves than wetter or clay-bearing earth materials. Therefore, signal penetration depths for this study reached upwards of 11 m. Similar observations regarding optimal conditions for GPR surveying in carbonates are discussed by Jorry & Bièvre (2011), where GPR was used to image carbonate platform features in the Paris Basin. However, unlike Jorry & Bièvre (2011) and others (Martinez *et al.* 1998; Aspiron & Aigner 2000; Aspiron *et al.* 2009; Menezes *et al.* 2016) who have dealt mainly with outcrop scale investigations of carbonates using GPR, this study has successfully extended the use of GPR to the regional-scale imaging of carbonates.

Logistically, the bike-trail across Bonaire provided unique access to a 3.9-km transect, something that is not always available in other field locations. Yet beyond the favourability of the site conditions for using GPR, the use of quantitative data analysis by means of *k*-means clustering of structure-parallel vectors allowed for semi-automatic determination of radar facies from the CIT survey. Classical studies have made use of manual tracing of GPR reflection patterns and geometries for geologic interpretation (Martinez *et al.* 1998; Aspiron & Aigner 2000; Aspiron *et al.* 2009; Bennett *et al.* 2009; Jorry & Bièvre 2011; Franke *et al.* 2015). Such methods may be beneficial for unambiguous reflection geometries and/or small-scale studies. However, these methods rely heavily on the skill, judgement and

prior experience of the interpreter and can be very time consuming for large data sets.

Measurements of the image texture have been used previously to provide data-driven interpretations of structural information in GPR data. A specific example in carbonate geology is the work by Menezes *et al.* (2016), where a grey-level cooccurrence matrix was used as a metric for GPR image texture. Image texture analysis has also been combined with clustering analysis in GPR data. In an investigative paper, Moysey *et al.* (2006) examined the use of many different measures of image texture, including variance, covariance, Fourier–Mellin transform, R-transform and Principal Component Analysis, to provide data-driven synthesis of GPR sections via neural network classification. Yet, such previously used measures of texture are simply proxies for reflection orientation. Structure-parallel vectors derived from structure tensors are an attribute that explicitly represents structural geometries of GPR reflections. By using structure-parallel vectors in a k -means clustering algorithm, the structural information from the regional-scale CIT was synthesized into a few clusters that were intuitively incorporated into a set of radar facies relating to geologic structures occurring on Bonaire. Furthermore, each cluster was investigated in terms of vector dip and vector linearity. Without the use of clustering, traditional methods of reflection tracing would have been tedious across the CIT, and reflection orientations within radar facies would not contain the quantitative information the clustering provides. The k -means routine used here is intuitive and allows for straightforward implementation. It also eliminates the need to build training data sets as would be required in methods such as neural networks. Structure-parallel attributes of GPR images can be readily utilized in more sophisticated methods such as fuzzy clustering and hierarchical clustering (Jain *et al.* 1999).

The methods used in this study highlight the ability to use GPR as a primary subsurface investigation tool for carbonate geologic mapping, even at large scales where high-resolution data sets can become cumbersome. In cases where large spatial scales are investigated, it is essential to efficiently synthesize data by means of methods such as automatic data segmentation or clustering in order to provide quantitative support for geologic interpretations.

6.4 Limitations of the study

The average depth of investigation for the GPR data along the CIT is 11 m. An interface between the carbonate platform cover and the volcanic basement would likely produce a strong reflection in the data due to the significantly different EM properties of volcanic and carbonate rocks (Telford *et al.* 1990; Olhoeft 1998). Since such a reflector at depth is absent along the whole of the CIT, we infer that the carbonate-basement contact was not imaged in this study, and exists deeper than 11 m below the surface. The specific morphology of this volcanic basement directly influences the carbonate platform development. Since GPR at 100 MHz is unable to image the basement contact, we suggest magnetic geophysical surveying (Grauch 2002; Wetmore *et al.* 2009; Robertson *et al.* 2017) as an appropriate means to provide new insights into effects that the original geometry of volcanic basement may have had on the development of the carbonate successions on Bonaire.

In addition, while this work has shown the utility that automatic data segmentation provides to radar facies analysis, the numerical techniques were unable to automatically classify radar facies in and of themselves. In this work, a manual interpretation of clusters into radar facies was still required. As the classification was performed

on the entire GPR data set, it is likely that unwanted migration artefacts contributed to the clustering results. This is evidenced by the presence of a significant amount of lower-linearity vectors in the cluster-dip distributions (Fig. 4). Also, while the use of the AGC-gained data set removed unwanted amplitude variations (mainly due to localized ground-coupling differences) from affecting the clustering results, relative amplitude information of GPR reflections due to geologic features were not included. This information had to be manually incorporated into the radar facies analysis (Fig. 6). Future work in applying the clustering to specific (i.e. artefact-free) windows of a GPR data set and incorporation of relative amplitude information may bring the results closer to a fully automatic classification of radar facies.

7 CONCLUSIONS

The island of Bonaire contains excellent exposures of carbonate successions that encode information relating to previous tectonic and eustatic conditions in the southern Caribbean. Through this study, we have examined plausible processes and environments of deposition that have formed the progradational platform units found on the island. GPR proved to be a useful tool to study the geological evolution of Bonaire due to the excellent exposures and the favourable conditions for signal penetration. Semi-automated facies classification using image structure tensors derived from the GPR data facilitated a detailed mapping and interpretation at the regional scale. Our identification of clearly defined progradational units occurring on the northeastern windward portion of the island illustrates a period of reduced accommodation space, thus forcing lateral shedding of sediments. We further reveal geometries related to the leeward portion of the platform. These include karstic features that we have correlated with lithology samples to environments of deposition conducive to dolimitization, transitional foreshore-to-shoreface geometries and high-angle beds, which likely correlate with deformation previously observed in the lower Seroe Domi Formation. This study has illustrated the use of GPR as a valuable tool for platform-scale investigation of carbonate geologies in settings such as Bonaire, and has provided additional insight into the complex dynamics of carbonate production in the southern Caribbean.

ACKNOWLEDGEMENTS

Data acquisition, methodology development, data processing and analysis and report writing for this work were performed by R.D. Bowling. J.C. Laya provided result analysis and review, and M.E. Everett provided additional technical review as well as project mentorship. Funding for this work was supported, in part, by the Howard Karren Professorship and Dr Juan Carlos Laya at Texas A&M University. The authors would like to thank T. deSmet and C. Stanford for their help in data acquisition and helpful comments on data analysis. Information regarding access to the raw GPR files (in .DT1/.HD format) for the CIT can be found in the Supporting Information for this paper, along with large format figures of the CIT and CIT-clustering results.

REFERENCES

- Alexander, C.S., 1961. The marine terraces of Aruba, Bonaire, and Curaçao, Netherlands Antilles, *Ann. Assoc. Am. Geogr.*, **51**, 102–123.
- Annan, A.P., 2009. Electromagnetic principles of ground penetrating radar, in *Ground Penetrating Radar Theory and Applications*, pp. 1–40, ed Jol, H.M., Elsevier.

- Annan, A.P., 2003. *Ground Penetrating Radar Principles, Procedure & Applications*, Sensors and Software.
- Annan, A.P., 1996. Transmission dispersion and GPR, *J. Environ. Eng. Geophys.*, **1**, 125–136.
- Annan, A.P., 1973. Radio interferometry depth sounding: part I—theoretical discussion, *Geophysics*, **38**, 557–580.
- Asprion, U. & Aigner, T., 2000. An initial attempt to map carbonate buildups using ground-penetrating radar: an example from the upper Jurassic of SW-Germany, *Facies*, **42**, 245–252.
- Asprion, U., Westphal, H., Nieman, M. & Pomar, L., 2009. Extrapolation of depositional geometries of the Menorcan Miocene carbonate ramp with ground-penetrating radar, *Facies*, **55**, 37–46.
- Bandoian, C.A. & Murray, R.C., 1974. Plio-pleistocene carbonate rocks of Bonaire, Netherlands Antilles, *Bull. geol. Soc. Am.*, **85**, 1243–1252.
- Bennett, M.R., Cassidy, N.J. & Pile, J., 2009. Internal structure of a barrier beach as revealed by ground penetrating radar (GPR): Chesil Beach, UK, *Geomorphology*, **104**, 218–229.
- Bowling, R., 2017. *Applications of Ground Penetrating Radar to Structural Analysis of Carbonate Terraces on the Island of Bonaire, Caribbean Netherlands*, Texas A&M University.
- Bradford, J.H., 2007. Frequency-dependent attenuation analysis of ground-penetrating radar data, *Geophysics*, **72**, J7–J16.
- Brandano, M. & Corda, L., 2002. Nutrients, sea-level and tectonics: constraints for the facies architecture of a Miocene carbonate ramp in central Italy, *Terra Nova*, **14**, 257–262.
- Bristow, C., 2009. Ground penetrating radar in Aeolian dune sands, in *Ground Penetrating Radar Theory and Applications*, pp. 271–297, ed Jol, H.M., Elsevier.
- Brookfield, M.E., 1977. The origin of bounding surfaces in ancient aeolian sandstones, *Sedimentology*, **24**, 303–332.
- Cai, X., Nie, F. & Huang, H., 2013. Multi-view K-means clustering on big data, in *Proceedings of the Twenty-Third International Joint Conference on Artificial Intelligence*, Beijing, China, pp. 2598–2604.
- Cassidy, N.J., 2009. Electrical and magnetic properties of rocks, soils and fluids, in *Ground Penetrating Radar Theory and Applications*, pp. 41–72, ed Jol, H.M., Elsevier.
- Claerbout, J.F., 1985. *Imaging the Earth's Interior*, Blackwell Scientific Publications.
- Davis, J.L. & Annan, A.P., 1989. Ground-penetrating radar for high-resolution mapping of soil and rock stratigraphy, *Geophys. Prospect.*, **37**, 531–551.
- de Buisonjé, P.H., 1974. *Neogene and Quaternary Geology of Aruba, Curaçao and Bonaire*, Universiteit Utrecht.
- de Buisonjé, P.H., 1964. Marine terraces and sub-aeric sediments on the Netherlands Leeward Islands, Curacao, Aruba, and Bonaire, as indications of Quaternary changes in sea level and climate, *Proc. K. Ned. Akad. Wet. B*, **67**, 60–79.
- de Kleine, M.P.E. & Bakker, M.A.J., 2009. Subsurface characterization in a karstified limestone area using ground-penetrating radar: Bonaire, Netherlands Antilles, in *Symposium on the Application of Geophysics to Engineering and Environmental Problems 2009*, pp. 489–498, Environmental and Engineering Geophysical Society, doi:10.4133/1.3176734.
- Deffeyes, K.S., Lucia, F.J. & Weylt, P.K., 1964. Dolomitization: observations on the island of Bonaire, Netherlands Antilles, *Science*, **143**, 678–679.
- Della Porta, G., Kenter, J.A.M. & Bahamonde, J.R., 2004. Depositional facies and stratal geometry of an upper carboniferous prograding and aggrading high-relief carbonate platform (Cantabrian Mountains, N Spain), *Sedimentology*, **51**, 267–295.
- Ding, C., Zhou, D., He, X. & Zha, H., 2006. R1-PCA: rotational invariant L1-norm principal component analysis for robust subspace factorization, in *Proceedings of the 23rd International Conference on Machine Learning - ICML'06*, ACM Press, New York, pp. 281–288.
- Du, L., Zhou, P., Shi, L., Wang, H., Fan, M., Wang, W. & Shen, Y.D., 2015. Robust multiple kernel K-means using L2,1-norm, in *Proceedings of the Twenty-Fourth International Conference on Artificial Intelligence*, Buenos Aires, Argentina, pp. 3476–3482.
- Dujardin, J.-R. & Bano, M., 2013. Topographic migration of GPR data: examples from Chad and Mongolia, *C. R. Geosci.*, **345**, 73–80.
- Eberli, G.P. & Ginsburg, R.N., 1989. Cenozoic progradation of northwestern Great Bahama Bank, a record of lateral platform growth and sea-level fluctuations, in *Controls on Carbonate Platforms and Basin Development*, pp. 339–351, SEPM (Society for Sedimentary Geology) Special publication, doi:10.2110/pec.89.44.0339.
- Everett, M.E., 2013. Ground-penetrating Radar, in *Near-Surface Applied Geophysics*, pp. 239–278, Cambridge University Press, doi:10.1017/CBO9781139088435.010.
- Farr, T.G. et al., 2007. The shuttle radar topography mission, *Rev. Geophys.*, **45**, RG2004, doi:10.1029/2005RG000183.
- Fehmers, G.C. & Höcker, C.F.W., 2003. Fast structural Interpretation with Structure-oriented filtering, *Geophysics*, **68**, 1286–1293.
- Forte, E., Pipan, M., Casabianca, D., Di Cuia, R. & Riva, A., 2012. Imaging and characterization of a carbonate hydrocarbon reservoir analogue using GPR attributes, *J. Appl. Geophys.*, **81**, 76–87.
- Fouke, B.W., Beets, C.J., Meyers, W.J., Hanson, G.N. & Melillo, A.J., 1996. ⁸⁷Sr/⁸⁶Sr Chronostratigraphy and dolomitization history of the Seroc Domi Formation, Curaçao (Netherlands Antilles), *Facies*, **35**, 293–320.
- Franke, D., Hornung, J. & Hinderer, M., 2015. A combined study of radar facies, lithofacies and three-dimensional architecture of an alpine alluvial fan (Illgraben fan, Switzerland), *Sedimentology*, **62**, 57–86.
- Gerlitz, K., Knoll, M.D., Cross, G.M., Luzitano, R.D. & Knight, R., 1993. Processing ground penetrating radar data to improve resolution of near-surface targets, in *Symposium on the Application of Geophysics to Engineering and Environmental Problems 1993*, pp. 561–574, Environmental and Engineering Geophysical Society, doi:10.4133/1.2922036.
- Golub, G.H. & Van Loan, C.F., 1996. Matrix analysis, in *Matrix Computations*, pp. 48–87, Johns Hopkins University Press.
- Grauch, V.J.S., 2002. *High-Resolution Aeromagnetic Survey to Image Shallow Faults, Dixie Valley Geothermal Field, Nevada*, US Geological Survey Publication.
- Griffiths, D.J., 1999. *Introduction To Electrodynamics*, 3rd edn, Prentice Hall.
- Hale, D., 2009. Structure-oriented smoothing and semblance, *CWP Rep.*, **635**, 261–270.
- Haq, B.U., Hardenbol, J. & Vail, P.R., 1987. Chronology of fluctuating sea levels since the Triassic, *Science*, **235**, 1156–1167.
- Hazard, C.S., Ritter, S.M., McBride, J.H., Tingey, D.G. & Keach, R.W., 2017. Ground-penetrating-radar characterization and porosity evolution of an upper pleistocene oolite-capped depositional cycle, red bays, Northwest Andros Island, Great Bahama Bank, *J. Sediment. Res.*, **87**, 523–545.
- Hippolyte, J.-C. & Mann, P., 2011. Neogene–quaternary tectonic evolution of the leeward Antilles Islands (Aruba, Bonaire, Curaçao) from fault kinematic analysis, *Mar. Pet. Geol.*, **28**, 259–277.
- Jain, A.K., 2010. Data clustering: 50 years beyond K-means, *Pattern Recognit. Lett.*, **31**, 651–666.
- Jain, A.K., Murty, M.N. & Flynn, P.J., 1999. Data clustering: a review, *ACM Comput. Surv.*, **31**, 264–323.
- James, N.P. & Jones, B., 2016. *Origin of Carbonate Rocks*, John Wiley & Sons Ltd.
- Jorry, S.J. & Bièvre, G., 2011. Integration of sedimentology and ground-penetrating radar for high-resolution imaging of a carbonate platform, *Sedimentology*, **58**, 1370–1390.
- Laya, J.C. et al., 2018. Controls on neogene carbonate facies and stratigraphic architecture of an isolated carbonate platform – the Caribbean island of Bonaire, *Mar. Pet. Geol.*, **94**, 1–18.
- Laya, J.C., Whitaker, F.F., Tucker, M. & Gabellone, T., 2017. Facies control on dolomitisation within the neogene succession of Bonaire, Netherlands Antilles, in *AAPG Annual Convention and Exhibition*, Houston, TX.
- Lehmann, F., Mühlh, D.V., van der Veen, M., Wild, P. & Green, A.G., 1998. True topographic 2-D migration of georadar data, in *Symposium on the Application of Geophysics to Engineering and Environmental Problems 1998*, pp. 107–114, Environmental and Engineering Geophysical Society, doi:10.4133/1.2922491.
- Lucia, F.J., 2007. *Carbonate Reservoir Characterization*, 2nd edn, Springer.
- Lucia, F.J., 1968. Recent sediments and diagenesis of South Bonaire, Netherlands Antilles, *SEPM J. Sediment. Res.*, **38**, 845–858.

- Lugo, A.E., Rogers, C.S. & Nixon, S.W., 2000. Hurricanes, coral reefs and rainforests: resistance, ruin and recovery in the Caribbean, *AMBIO A J. Hum. Environ.*, **29**, 106–114.
- Kenter, J.A.M., 1990. Carbonate platform flanks: slope angle and sediment fabric, *Sedimentology*, **37**, 777–794.
- MacQueen, J., 1967. Some methods for classification and analysis of multivariate observations, in *Proceedings of the Fifth Berkeley Symposium on Mathematical Statistics and Probability*, pp. 281–297, eds Lecam, L.M. & Neyman, J., University of California Berkeley Press, Oakland, CA.
- Martinez, A., Kruger, J.M. & Franseen, E.K., 1998. Utility of ground-penetrating radar in near-surface, high-resolution imaging of Lansing-Kansas City (Pennsylvanian) limestone reservoir analogs, *Kansas Geol. Surv. Bull.*, **241**, 43–59.
- Menezes, P.T.L., Travassos, J.M., Medeiros, M.A.M. & Takayama, P., 2016. High-resolution facies modeling of presalt lacustrine carbonates reservoir analog: morro do chaves formation example, Sergipe-Alagoas Basin, Brazil, *Interpretation*, **4**, SE63–SE74.
- Mitchum, R.M., Jr., Vail, P.R. & Sangree, J.B., American Association of Petroleum Geologists, Payton, C.E., 1977. Seismic stratigraphy and global changes of sea level, part six: stratigraphic interpretation of seismic reflection patterns in depositional sequences, in *Seismic Stratigraphy — Applications to Hydrocarbon Exploration*, pp. 117–134.
- Moysey, S., Knight, R.J. & Jol, H.M., 2006. Texture-based classification of ground-penetrating radar images, *Geophysics*, **71**, 111–118.
- Muhs, D.R., Pandolfi, J.M., Simmons, K.R. & Schumann, R.R., 2012. Sea-level history of past interglacial periods from uranium-series dating of corals, Curaçao, Leeward Antilles Islands, *Quat. Res.*, **78**, 157–169.
- Mutti, M., Bernoulli, D., Eberli, G.P. & Vecsei, A., 1996. Depositional geometries and facies associations in an upper Cretaceous prograding carbonate platform margin (Orfento Supersequence, Maiella, Italy), *SEPM J. Sediment. Res.*, **66**, 749–765.
- Mutti, M., Bernoulli, D. & Stille, P., 1997. Temperate carbonate platform drowning linked to Miocene oceanographic events: Maiella platform margin, Italy, *Terra Nova*, **9**, 122–125.
- Mylroie, J.E. & Carew, J.L., 1995. Karst development on carbonate islands, in *Unconformities in Carbonate Strata—Their Recognition and the Significance of Associated Porosity*, *AAPG Memoir*, 55–76, eds Budd, D.A., Saller, A.H. & Harris, P.A., AAPG.
- Neal, A., 2004. Ground-penetrating radar and its use in sedimentology: principles, problems and progress, *Earth-Sci. Rev.*, **66**, 261–330.
- Olhoeft, G.R., 1998. Electrical, magnetic, and geometric properties that determine ground penetrating radar performance, in *Seventh Int'l Conf. on Ground Penetrating Radar*, Lawrence, KS, pp. 177–182.
- Pijpers, P.J., 1933. *Geology and Paleontology of Bonaire*, Utrecht University.
- Pomar, L., 2001. Types of carbonate platforms: a genetic approach, *Basin Res.*, **13**, 313–334.
- Pomar, L., Esteban, M., Martinez, W., Espino, D., Castillo de Ott, V., Benkovics, L. & Castro Leyva, T., 2015. Oligocene-Miocene carbonates of the Perla field, offshore Venezuela: depositional model and facies architecture, in *Petroleum Geology and Potential of the Colombian Caribbean Margin*, *AAPG Memoir*, pp. 647–673, eds Bartolin, C. & Mann, P., AAPG.
- Pomar, L. & Hallock, P., 2008. Carbonate factories: a conundrum in sedimentary geology, *Earth-Sci. Rev.*, **87**, 134–169.
- Read, J.F., 1995. Overview of carbonate platform sequences, cycle stratigraphy and reservoirs in greenhouse and Ice-House worlds, in *Milankovitch Sea-Level Changes, Cycles, and Reservoirs on Carbonate Platforms in Greenhouse and Ice-House Worlds (SC35)*, pp. 1–102, eds Read, J.F., Kerans, C., Weber, L.J., Sarg, J.F. & Wright, F.M., SEPM (Society for Sedimentary Geology), doi:10.2110/scn.95.35.0001.
- Reams, R., 1999. Hadamard inverses, square roots and products of almost semidefinite matrices, *Linear Algebr. Appl.*, **288**, 35–43.
- Reijmer, J.J., Betzler, C., Kroon, D., Tiedemann, R. & Eberli, G.P., 2002. Bahamian carbonate platform development in response to sea-level changes and the closure of the Isthmus of Panama, *Int. J. Earth Sci.*, **91**, 482–489.
- Reynolds, J.M., 1997. *An Introduction to Applied and Environmental Geophysics*, 1st edn, John Wiley & Sons Ltd.
- Robertson, D.J., Vidanovich, P.N.P., Zoellner, S.K. & Meyers, J.B., 2017. Interpretation of aeromagnetic data in the Franklin area, northern New Zealand, *N.Z. J. Geol. Geophys.*, **60**, 36–50.
- Schellmann, G., Radtke, U., Scheffers, A., Whelan, F. & Kelletat, D., 2004. ESR dating of coral reef terraces on Curaçao (Netherlands Antilles) with estimates of younger Pleistocene sea level elevations, *J. Coast. Res.*, **204**, 947–957.
- Schlager, W., Reijmer, J.J.G. & Droxler, A., 1994. Highstand shedding of carbonate platforms, *J. Sediment. Res.*, **B64**, 270–281.
- Sensors and Software Inc., 2016. EKKO.Project.
- Shanov, S. & Kostov, K., 2015. Tectonic control on karst evolution, in *Dynamic Tectonics and Karst*, pp. 1–5, Springer.
- Smart, P.L., Dawans, J.M. & Whitaker, F., 1988. Carbonate dissolution in a modern mixing zone, *Nature*, **335**, 811–813.
- Smith, D.G. & Jol, H.M., 1995. Ground penetrating radar: antenna frequencies and maximum probable depths of penetration in Quaternary sediments, *J. Appl. Geophys.*, **33**, 93–100.
- Steinley, D., 2006. K-means clustering: a half-century synthesis, *Br. J. Math. Stat. Psychol.*, **59**, 1–34.
- Stoffers, A.L., 1956. *The Vegetation of the Netherlands Antilles*, Utrecht.
- Sulacia, J., Laya, J.C. & Tucker, M.E., 2015. Analysis of carbonate isolated platform, geometries and facies distribution of Pleistocene carbonates in Bonaire, southern Caribbean, in *AAPG Annual Convention and Exhibition*, Denver, CO.
- Sulaica, J., 2015. *Facies Distribution and Paleogeographic Evolution of Neogene Carbonates in Bonaire, Netherlands Antilles*, Texas A&M University.
- Telford, W., Geldart, L. & Sheriff, R., 1990. Electrical properties of rocks and minerals, in *Applied Geophysics*, pp. 283–292, Cambridge University Press.
- Tucker, M.E. & Wright, P.V., 1990. Carbonate mineralogy and chemistry, in *Carbonate Sedimentology*, pp. 284–313, Blackwell Publishing Ltd.
- Vail, P.R., 1987. Seismic stratigraphy interpretation using sequence stratigraphy part I: seismic stratigraphy interpretation procedure, *AAPG Stud. Geol.*, **1**, 1–10.
- Van der Hilst, R. & Mann, P., 1994. Tectonic implications of tomographic images of subducted lithosphere beneath northwestern South America, *Geology*, **22**, 451–454.
- Van Vliet, L. & Verbeek, P., 1995. Estimators for orientation and anisotropy in digitized images, in *Proceedings of the First Conference of the Advanced School for Computing and Imaging*, pp. 442–450, Advanced School for Computing and Imaging, Heijlen, The Netherlands.
- Weickert, J., 1995. Multiscale texture enhancement, in *Proceedings Computer Analysis of Images and Patterns, 6th International Conference, CAIP '95 Prague, Czech Republic*, pp. 230–237, doi:10.1007/3-540-60268-2_301.
- Westermann, J.H. & Zonneveld, J.I.S., 1956. Photo-geological observations and land capability & land use survey of the island of Bonaire, Netherlands Antilles. No. 123. Koninklijk Instituut voor de Tropen, 1956.
- Wetmore, P.H., Connor, C.B., Kruse, S.E., Callihan, S., Pignotta, G., Stremtan, C. & Burke, A., 2009. Geometry of the Trachyte Mesa intrusion, Henry Mountains, Utah: Implications for the emplacement of small melt volumes into the upper crust, *Geochem. Geophys. Geosyst.*, **10**, doi:10.1029/2009GC002469.
- Yilmaz, Ö., 2001. *Seismic Data Analysis*, Society of Exploration Geophysicists, doi:10.1190/1.9781560801580.

SUPPORTING INFORMATION

Supplementary data are available at [GJI](#) online.

Figure S1. Topographically migrated cross-island transect, $x = 0$ –200 m. (a) Power-law-gained data. (b) AGC-gained data. Locator map in centre showing location of section (red box) in relation to entire line (cyan line). Vertical exaggeration of sections, $4\times$. Vertical exaggeration of locator map, $9.3\times$.

Figure S2. Topographically migrated cross-island transect, $x = 200.2$ –600.2 m. (a) Power-law-gained data. (b) AGC-gained

data. Locator map in centre showing location of section (red box) in relation to entire line (cyan line). Vertical exaggeration of sections, 4×. Vertical exaggeration of locator map, 9.3×.

Figure S3. Topographically migrated cross-island transect, $x = 600.4\text{--}1000.4$ m. (a) Power-law-gained data. (b) AGC-gained data. Locator map in centre showing location of section (red box) in relation to entire line (cyan line). Vertical exaggeration of sections, 4×. Vertical exaggeration of locator map, 9.3×.

Figure S4. Topographically migrated cross-island transect, $x = 712\text{--}1112$ m. (a) Power-law-gained data. (b) AGC-gained data. Locator map in centre showing location of section (red box) in relation to entire line (cyan line). Vertical exaggeration of sections, 4×. Vertical exaggeration of locator map, 9.3×.

Figure S5. Topographically migrated cross-island transect, $x = 1112.2\text{--}1512.2$ m. (a) Power-law-gained data. (b) AGC-gained data. Locator map in centre showing location of section (red box) in relation to entire line (cyan line). Vertical exaggeration of sections, 4×. Vertical exaggeration of locator map, 9.3×.

Figure S6. Topographically migrated cross-island transect, $x = 1512.4\text{--}1912.4$ m. (a) Power-law-gained data. (b) AGC-gained data. Locator map in centre showing location of section (red box) in relation to entire line (cyan line). Vertical exaggeration of sections, 4×. Vertical exaggeration of locator map, 9.3×.

Figure S7. Topographically migrated cross-island transect, $x = 1912.6\text{--}2312.6$ m. (a) Power-law-gained data. (b) AGC-gained data. Locator map in centre showing location of section (red box) in relation to entire line (cyan line). Vertical exaggeration of sections, 4×. Vertical exaggeration of locator map, 9.3×.

Figure S8. Topographically migrated cross-island transect, $x = 2312.8\text{--}2712.8$ m. (a) Power-law-gained data. (b) AGC-gained data. Locator map in centre showing location of section (red box) in relation to entire line (cyan line). Vertical exaggeration of sections, 4×. Vertical exaggeration of locator map, 9.3×.

Figure S9. Topographically migrated cross-island transect, $x = 2713\text{--}3113$ m. (a) Power-law-gained data. (b) AGC-gained data. Locator map in centre showing location of section (red box) in relation to entire line (cyan line). Vertical exaggeration of sections, 4×. Vertical exaggeration of locator map, 9.3×.

Figure S10. Topographically migrated cross-island transect, $x = 3131.2\text{--}3513.2$ m. (a) Power-law-gained data. (b) AGC-gained data. Locator map in centre showing location of section (red box) in relation to entire line (cyan line). Vertical exaggeration of sections, 4×. Vertical exaggeration of locator map, 9.3×.

Figure S11. Topographically migrated cross-island transect, $x = 3400\text{--}3800$ m. (a) Power-law-gained data. (b) AGC-gained data. Locator map in centre showing location of section (red box) in relation to entire line (cyan line). Vertical exaggeration of sections, 4×. Vertical exaggeration of locator map, 9.3×.

Figure S12. Topographically migrated cross-island transect, $x = 3800\text{--}3900$ m. (a) Power-law gained data. (b) AGC-gained data. Locator map in centre showing location of section (red box) in relation to entire line (cyan line). Vertical exaggeration of sections, 4×. Vertical exaggeration of locator map, 9.

Figure S13. Clustering results: $x = 0\text{--}200$ m. Vertical exaggeration 4×. Locator map on showing section displayed indicated by red box.

Figure S14. Clustering results: $x = 200.2\text{--}600.2$ m. Vertical exaggeration 4×. Locator map on showing section displayed indicated by red box.

Figure S15. Clustering results: $x = 600.4\text{--}1000.4$ m. Vertical exaggeration 4×. Locator map on showing section displayed indicated by red box.

Figure S16. Clustering results: $x = 712\text{--}1112$ m. Vertical exaggeration 4×. Locator map on showing section displayed indicated by red box.

Figure S17. Clustering results: $x = 1112.2\text{--}1512.2$ m. Vertical exaggeration 4×. Locator map on showing section displayed indicated by red box.

Figure S18. Clustering results: $x = 1512.4\text{--}1912.4$ m. Vertical exaggeration 4×. Locator map on showing section displayed indicated by red box.

Figure S19. Clustering results: $x = 1912.6\text{--}2312.6$ m. Vertical exaggeration 4×. Locator map on showing section displayed indicated by red box.

Figure S20. Clustering results: $x = 2312.8\text{--}2712.8$ m. Vertical exaggeration 4×. Locator map on showing section displayed indicated by red box.

Figure S21. Clustering results: $x = 2713\text{--}3113$ m. Vertical exaggeration 4×. Locator map on showing section displayed indicated by red box.

Figure S22. Clustering results: $x = 3113\text{--}3513.2$ m. Vertical exaggeration 4×. Locator map on showing section displayed indicated by red box.

Figure S23. Clustering results: $x = 3400\text{--}3800$ m. Vertical exaggeration 4×. Locator map on showing section displayed indicated by red box.

Figure S24. Clustering results: $x = 3800.2\text{--}3900$ m. Vertical exaggeration 4×. Locator map on showing section displayed indicated by red box.

Please note: Oxford University Press is not responsible for the content or functionality of any supporting materials supplied by the authors. Any queries (other than missing material) should be directed to the corresponding author for the paper.

APPENDIX: k -MEANS CLUSTERING ALGORITHM ADAPTED FOR PATCHES OF STRUCTURE-PARALLEL VECTORS

A basic k -means algorithm can be written as follows (Steinley 2006):

Given a set of N vectors, (1) initially choose k vectors that represent the mean-vectors of k clusters. (2) For each vector in N , compute the distance to each mean-vector in k . (3) Assign the current vector to the cluster whose mean-vector is closest. (4) After all vectors in N have been assigned, compute the new mean-vectors of each cluster. (5) Repeat (2)–(4) until the mean-vectors do not change significantly between iterations.

A given patch of structure-parallel vectors is defined as a 3-D matrix, \mathbf{X} , with dimensions $n \times m \times 2$, where X_1 is a matrix containing the first elements in each of the associated structure-parallel vectors and X_2 is a matrix containing the second elements in the vectors. A visual example of a 3×3 patch of structure-parallel vectors is shown in Fig. 3(b).

In order to compute a measure of closeness between patches of structure-parallel vectors (as is necessary for steps 2–3 of the k -means algorithm), we define the distance, D , between two patches of structure-parallel vectors, \mathbf{X} and \mathbf{M} , as the $L_{2,1}$ -norm (Ding *et al.* 2006; Cai *et al.* 2013; Du *et al.* 2015) of the matrix of element-wise Euclidean norms between \mathbf{X} and \mathbf{M} (Bowling 2017),

$$D(\mathbf{X}, \mathbf{M}) = \left\| \left(\sum_{l=1}^2 (X_l - M_l)^2 \right)^{1/2} \right\|_{2,1}, \quad (\text{A1})$$

where the expression inside the double bars describes a matrix of Euclidean norms between the vectors associated with patches \mathbf{X} and \mathbf{M} . The computation of these element-wise Euclidean norms is facilitated by the use of the Hadamard power operator \circ (Reams 1999). Hadamard power operators act on the elements of a matrix rather than on a matrix as a whole.

The exit criterion for the k -means algorithm (step 5 above) requires the comparison of each cluster's current mean to the cluster's mean at the previous iteration. This was accomplished in this work by computing the change in a given mean, \mathbf{M} , between iterations $n - 1$ and n as the measure of the relative error (Golub & Van Loan 1996) between \mathbf{M}_{n-1} and \mathbf{M}_n ,

$$\frac{D(\mathbf{M}_{n-1}, \mathbf{M}_n)}{D(\mathbf{M}_n)}, \quad (\text{A2})$$

with D being defined as in eq. (A1). Note that for the denominator of eq. (A2), this distance metric operates on a single patch as a norm. The use of relative error means that this metric is independent of the number of individual structure-parallel vectors in \mathbf{M} . The k -means clustering algorithm now terminates when the maximum change across all cluster means,

$$\Delta(n)_{\max} = \max \left\{ \frac{D(\mathbf{M}_{i,n-1}, \mathbf{M}_{i,n})}{D(\mathbf{M}_{i,n})}, \dots, \frac{D(\mathbf{M}_{k,n-1}, \mathbf{M}_{k,n})}{D(\mathbf{M}_{k,n})} \right\}, \quad (\text{A3})$$

falls below some user-defined tolerance (Bowling 2017), where $\mathbf{M}_{i,n}$ is the patch representing the mean of cluster i for $i = 1, \dots, k$ at iteration n .

With the above definitions and considerations, a k -means clustering algorithm that is adapted for use with patches of structure-parallel vectors can be described as follows (Bowling 2017):

Given a field of N structure-parallel vectors: (1) Initially choose k patches of vectors of size $n \times m$ that each represent a mean-patch, \mathbf{M} , of k clusters. (2) For each vector, \mathbf{x} , in N , compute the distance between a patch of $n \times m$ vectors, \mathbf{X} , centred on \mathbf{x} , to each mean-patch in k using eq. (A1). (3) Assign \mathbf{x} to the cluster whose mean-patch is closest to \mathbf{X} . (4) After all vectors in N have been assigned, compute the new mean-patch of each cluster through element-wise averages of vectors in the patches assigned to each cluster. (5) Iterate (2)–(4) until the maximum change across all cluster means, $\Delta(n)_{\max}$ [as per eq. (A3)], falls below some tolerance.

This algorithm was implemented in MATLAB and run using resources at the Texas A&M High Performance Research Computing center. Currently, the algorithm has a serial implementation and runs on a single node. The serial implementation clustered the full CIT in 51 h of computational time.